Late Pleistocene hydrological settings at world heritage Tsodilo Hills (NW Kalahari, Botswana), a site of ancient human occupation

Marielle Geppert [a,*], Frank Riedel [a], Venise S. Gummersbach [a], Stine Gutjahr [a], Philipp Hoelzmann [a], Maria D. Reyes Garzón [a], Elisha M. Shemang [b], Kai Hartmann [a]

[a] Department of Earth Sciences, Freie Universität Berlin, Berlin, Germany
[b] Department of Earth and Environmental Science, Botswana International University of Science & Technology, Palapye, Botswana

A B S T R A C T

Based on genetic studies, a Pleistocene Kalahari "palaeo-wetland", which spanned the region of the Okavango Delta and the Makgadikgadi Basin, was recently considered the geographic origin of evolutionary modern humans. It was proposed that subsequent out-of-homeland migration was induced by climate shifts. The Tsodilo Hills, which are in relative proximity to the Okavango Delta, represent a site of ancient human occupation since at least 100 ka. Local hydrological dynamics were predominantly controlled by climate variability and are archived in the sediments of Palaeolake Tsodilo. This study seeks to better understand the Late Pleistocene environments of the ancient Tsodilo people with a focus on palaeo-hydrological settings, which played a major role for their livelihoods.

Our multidisciplinary approach included different remote sensing and geophysical methods, comprehensive application of differential GPS, and sedimentological analyses concentrating on the lake beds. Four palaeo-shorelines could be identified, three of which indicate highstands during which the Tamacha palaeo-river drained Palaeolake Tsodilo towards the Okavango Panhandle. Two highstands during MIS 3b and LGM are related to periods of largely increased fish consumption by humans as has been documented by archaeologists. The palaeolake was likely most extended about 100 ka ago or earlier, when it covered ca. 70 km^2 and was 16 m deep. A single (neo-)tectonic fault could be detected.

We assume that the Tamacha palaeo-river was a gateway for ancient humans to reach the Tsodilo Hills from these palaeo-wetlands. The people took advantage of the Tsodilo Hills as shelter from weather hazards and as a natural fortress against predators and elephants. Geologically, the Tsodilo Hills were comparatively calm. They represented a relatively safe haven where the social behaviour of early modern humans could evolve to a higher complexity, which relates to the fundamental question when and where modern human behaviour began.

1. Introduction

The southern African Kalahari was recently considered the cradle of humankind (Chan et al., 2019), which was based on genetic studies and triggered controversial discussion (Gibbons, 2019) in respect of methodology but also against the background that specific palaeontological and archaeological evidence for the suggested interval from ca. 240–165 ka (Chan et al., 2019) is lacking (Robbins et al., 2016). *Homo sapiens* fossils from Morocco and South Africa dated to about 350–260 ka are rather considered a "pre-modern" evolutionary phase (Stringer and Galway-Witham, 2017) and thus estimation of split-time of African human genetic lineages is currently the most promising approach to frame the temporal origin of modern humans (e.g. Tishkoff et al., 2009). "Living human mitochondrial DNA haplotypes coalesce ~200,000 years ago" (Weaver, 2012). Although the African origin of our species is largely undisputed, it has never been established from which region we came. Eastern, southern and central Africa have all been proposed (e.g. Henn et al., 2011; Rito et al., 2019). A challenging idea is that modern *Homo sapiens* actually emerged within the interactions of many different populations across Africa (Scerri et al., 2018).

Tishkoff et al. (2009) suggested a potential shared ancestry of central African Pygmies and Khoisan-speaking people and considered the origin of modern humans' migration in southwestern Africa, near the coastal border of Namibia and Angola (Fig. 1 circle 1). Interestingly, this area is
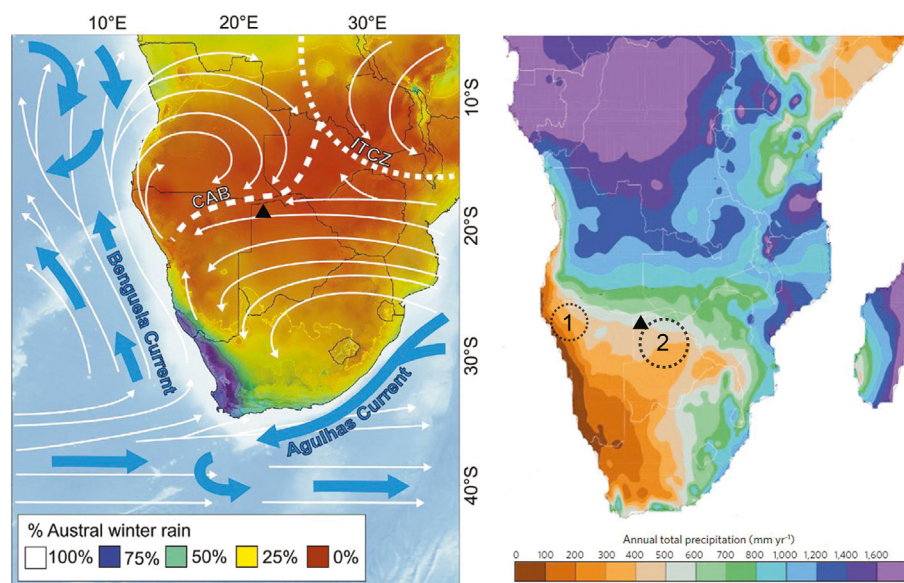
Fig. 1. Position of Tsodilo Hills (black triangle) in the modern southern African climate setting. Left: Major atmospheric (white arrows) and oceanic (blue arrows) circulation systems are shown as well as austral summer positions of ITCZ and Congo Air Boundary (CAB). Predominant (≥50%) austral winter rainfall is confined to violet to green coloured areas (permission for the use of artwork granted from Chevalier and Chase, 2016). Right: Zonation of mean annual precipitation (after Conway et al., 2015). Circles outline areas from where earliest modern humans may have originated (1 = Tishkoff et al., 2009; 2 = Chan et al., 2019).

in relative proximity to the Kalahari comprising the "Makgadikgadi-O-kavango palaeo-wetland" pinpointed by Chan et al. (2019; Fig. 1 circle 2). This area is nowadays semi-arid and has a pronounced seasonality with dry winters and wet summers (Peel et al., 2007; Gasse et al., 2008; Chevalier and Chase 2016, Fig. 1). The trivial truth is that human occupation did require sufficient nutrition, potable water and shelters. For a mega-lake spanning the Makgadikgadi Basin (Fig. 2) during ca. 100 ka, Schmidt et al. (2017) reconstructed alkaline and oligohaline water, not suitable for human consumption. A couple of (palaeo-)rivers, however, must have been active to have sustained such a huge lake and thus it can be assumed that potable water was relatively abundant.

Permanent natural and freely accessible sources of potable water are found further in the north, with the Kunene, Cubango-Okavango, Cuando-Linyanti-Chobe and Zambezi river systems (Fig. 2), encompassing both of the suggested origin areas (Tishkoff et al., 2009; Chan et al., 2019). The active head waters of these rivers are in the (semi-)humid tropics (Burrough et al., 2009; Riedel et al., 2014, Fig. 2), and taking long-term periodical migration of the ITCZ into consideration (McGee et al., 2014; Schneider et al., 2014), still perennial conditions should have prevailed during the rise of modern humans, and beyond. Ancient human dispersal is commonly related to climate change (Blome et al., 2012; Timmermann and Friedrich, 2016; Heine, 2019). Rito et al. (2019) concluded that during the last ca. 200 ka only soon after 70 ka, the climate was humid enough for human migrations between southern and eastern Africa and subsequent out-of-Africa expansions. Outside the humid tropics, stable environments were rather the exception, however, and landscape evolution was dynamic (Burrough, 2016). Huge lakes repeatedly existed in the structural basins of the northern and central Kalahari (Fig. 2) during the last 200 ka and before, which is that lakes developed, vanished and reappeared under changing climates (e.g. Grove, 1969; Heine, 1982; Burrough et al., 2009; Riedel et al., 2014; Schmidt et al., 2017; Heine, 2019). The structural basins of the Kalahari evolved with the southwestern spread of the East African Rift System (Modisi et al., 2000; Kinabo et al., 2007; Shemang and Molwalefhe, 2011). Water availability in this area therefore does not solely depend on climate but also on tectonic processes, vividly exemplified by the structural redirection of the Cuando-Linyanti-Chobe river system (Riedel et al., 2014, Fig. 2). On the one hand, absence or presence of lakes in the extended depressions of the Makgadikgadi-Okavango-Zambezi Basin (Ringrose et al., 2008, Fig. 2) do not necessarily reflect climate dynamics, and on the other hand the regional climate must not be in phase with evolution of lakes primarily controlled by remote active catchments.

It can tentatively be summarized that aridity prevailed in the Kalahari during the last ca. 200 ka, and more humid periods were rather exceptional (e.g. Brook et al., 1996; Burrough et al., 2009; Blome et al., 2012). A predominately arid climate concurs with special adaptations of Khoisan-speaking people, including traits which are absent in other human groups such as the ability to store water and lipid metabolites in body tissues (Schuster et al., 2010). These evolutionary adaptations indicate, however, that the small populations of Khoisan-speaking people living in the Kalahari (Bushmen or San) do not represent relicts of earliest modern humans but are descendants as well. Oldest (ca. 100 ka) direct evidence for modern human behaviour in southern Africa comes from Blombos Cave, located on the South African coast (Henshilwood et al., 2011) in the year-round rainfall zone (Chase and Meadows, 2007). The cave does not archive a permanent cultural record from the Middle into the Late Stone Age, though (Henshilwood et al., 2011). A site of permanent human occupation during the last ca. 100 ka does exist in the northern Kalahari (Robbins et al. 1994, 2000, 2010, 2016). These people inhabited rock shelters of the Tsodilo Hills (Fig. 3), inselbergs in proximity to the Okavango wetlands (Fig. 2) and which became UNESCO World Heritage Site in 2001 due to its outstanding rock art and its exceptionally long human occupation (Segadika, 2006). The Tsodilo Hills are more or less in the area where Chan et al. (2019) suspected the cradle of modern humans. Chan et al. (2019) proposed that out-of-homeland migration was induced by regional shifts in climate, shaping the genetic diversity of humans.

The Late Pleistocene climate variability is directly reflected by the dynamics of a fluvio-lacustrine system with lake formation along the western cliffs of the Tsodilo Hills. The drainage basin does not extend more than 120 km to the west (Fig. 2b), is therefore primarily controlled by local to regional climate, and lithospheric fracturing and seismicity are much lower compared to the Okavango Rift Zone (Hutchins et al., 1976; Nthaba et al., 2018; Ntibinyane et al., 2019). The lake basin is dry nowadays and the dynamics of the palaeo-lake have been discussed controversially (Brook et al.. 1992, 2010; Thomas et al., 2003; Wiese et al., 2020). Sediments from this "Palaeolake Tsodilo" were dated from ca. 43 ka (Wiese et al., 2020; this study) to approximately the Early Holocene (Thomas et al., 2003; Brook, 2010; Robbins and Murphy 2011). The sedimentary archive thus comprises the transition from the Middle to the Late Stone Age (McCall and Thomas, 2009; Robbins and Murphy, 2011; Villa et al., 2012).

Robbins et al. (2010) emphasized the importance of fishing for the ancient people of Tsodilo, at equal rank with hunting game. The bones of

Fig. 2. a) DEM of the Kalahari drainage system with position of Tsodilo Hills (after Riedel et al., 2014). Mean annual precipitation and temperature for indicated settlements are compiled in Table A.1; b) Extension of the drainage basin west of Tsodilo Hills, which is in the focus of this study (after Wiese et al., 2020).

cichlid freshwater fishes were found abundantly in cultural layers of the White Paintings Shelter located at the base of the Male Hill (Robbins et al., 2016, Fig. 3) and therefore at least periodically close to the shore of the palaeolake (Fig. A.8). Cichlids are tropical freshwater fish with low salinity tolerance (e.g. Salzburger and Meyer, 2004; Sparks and Smith, 2005). This implies that ancient people from Tsodilo either caught them from rivers such as the Ncamasere (Fig. 2b), which flowed north of the Tsodilo Hills into the Okavango still in historical times (Robbins et al., 1994; Brook, 2010) or from Palaeolake Tsodilo if it was not saline but contained freshwater. Gastropod and diatom assemblages from lake sediments rather point at periodically low salinities (Thomas et al., 2003; Wiese et al., 2020). This corresponds with a palaeo-outflow at the southern flank of the Male Hill (Fig. 3), which was active at least during lake highstands (Wiese et al., 2020; this study). On the other hand, neither hippopotamuses nor crocodiles seem to have ever reached Palaeolake Tsodilo, which is e.g. in contrast to other regional rather unstable lakes such as Ngami (Spinage, 2012, Fig. 2). The question, which role Palaeolake Tsodilo may have played for ancient people's

livelihoods remains unanswered. A closer look at palaeo-hydrological settings probably helps to better understand whether the lake itself may have promoted human occupation of the Tsodilo Hills since the Middle Stone Age or whether the hydroclimate under which the lake could develop was more important. The small number of 70–80 extant Khoisan-speaking people, which could sustain on potable water from wells hidden in the Tsodilo Hills until they were removed from their sacred place two decades ago (after declaration of Tsodilo Hills as UNESCO World Heritage site in 2001, personal communication), may provide a rough idea about past population sizes under a dry climate. It further suggests that ancient migration to the north (e.g. Rito et al., 2019), towards the tropical rain belt, was rather triggered by increasing aridity and not by increasing humidity when likely larger populations could occupy the Tsodilo Hills.

The aim of our study is to reconstruct stages of the fluvio-lacustrine system at the Tsodilo Hills with a multi-methodological approach focusing on lake evolution during ca. 43–19 ka. We test whether our results correspond with local archaeological evidence and human-
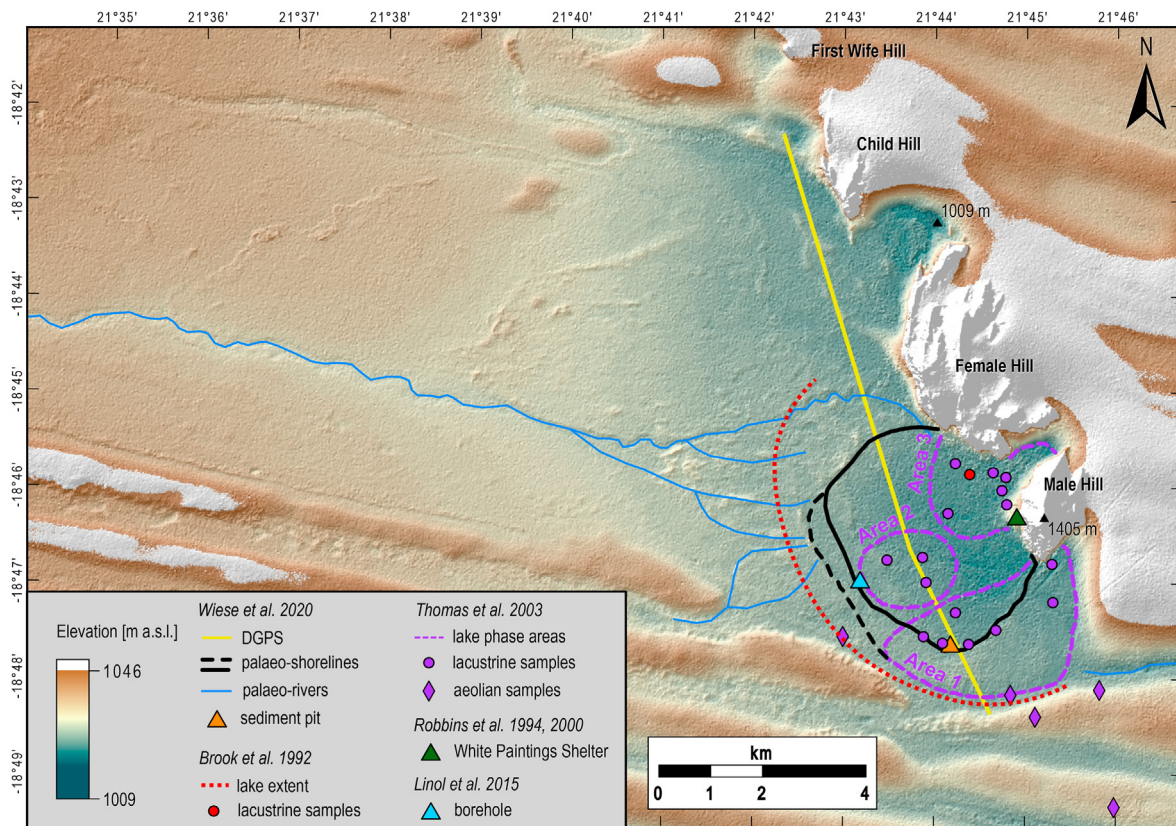
Fig. 3. TanDEM-X DEM of the study area showing the palaeolake depressions west of the Tsodilo Hills and sampling locations of previous studies with corresponding assumed palaeolake extensions (Brook, 1992; Robbins et al., 1994, 2000; Thomas et al., 2003; Wiese et al., 2020).

environment interaction respectively, and attempt to promote the discussion about subsistence strategies, that is e.g. local versus regional fishing. Our hydrological interpretations will be briefly compared with contemporary hydroclimate signals inferred from other archives across the northern and central Kalahari and beyond.

2. Study area

The Tsodilo Hills are a group of five Neoproterozoic, ca. 12 km NW to SE trending inselbergs composed of metasedimentary, kyanite-grade quartz-muscovite schists and ferruginous quartzites (Key and Ayres, 2000; Singletary et al., 2003; Wendorff, 2005). The individual hills have traditional names (Campbell 2010) with the "Female" most wide-ranging and the "Male" with the highest peak (1405 m a.s.l.; Fig. 3). The northern tip of the hill chain is located little more than 6 km south of the Nca-masere river valley (Fig. 2b). The landscape to the west of Child, Female and Male Hills (Fig. 3) shows little relief and comprises features of a former fluvio-lacustrine system, which levels at ca. 1010 m a.s.l. near the inselbergs (Grove, 1969; Brook, 2010; Wiese et al., 2020, Fig. 3). We refer to the lacustrine sub-system as Palaeolake Tsodilo.

Beyond the flat area, linear dunes, which are spaced ca. 1.5–2 km apart, trend from WNW to ESE (Fig. 3). In proximity to the Tsodilo Hills, the somewhat rounded dune crests rise about 20–30 m above the inter-dune areas (Grove, 1969; this study). Sand has piled up at the eastern flanks of the Tsodilo Hills indicating the major wind direction during dune formation and the wind-shadow position of the Palaeolake Tsodilo depressions (Brook, 2010; this study). Thomas et al. (2003) provided OSL-dated samples from two longitudinal dunes in a range from 107 to 23 ka. The so far oldest reconstructed lake highstand during ca. 43–41 cal ka BP, however, eroded the dunes (Wiese et al., 2020) indicating that OSL-dates younger than that reflect reworking of dune crests. The age of

the extended Northern Kalahari fields of linear dunes has been discussed in a wide range, from "Late Tertiary" (Cooke, 1980) to "Late Quaternary" (e.g. Chase, 2009; Thomas and Burrough, 2016; cf. Discussion). Brook et al. (1992), Thomas et al. (2003) and Wiese et al. (2020) all focused on the southern area of the palaeolake (Fig. 3). Their chronologies of lake phases are not in line. Thomas et al. (2003) presented surface sample (see Fig. 3) dates from ca. 41 to 8 cal ka BP indicating site-specific differences in lake bed erosion. The surface or near-surface sediments of the palae-olake depressions are characterized by carbonatic duricrusts (Brook et al., 1992; Thomas et al., 2003; Wiese et al., 2020). Wiese et al. (2020) assigned a potential palaeo-outflow to the east, ca. 2 km south of Male Hill (Fig. 3). The vegetation is generally considered the sandveld type (De Wit and Bekker, 1990; Bekker and De Wit, 1991), that is open grass- and shrubland with clusters of trees such as *Acacia* and *Terminalia* (cluster-leaf) (e.g. Cole and Brown, 1976; cf. van Wyk and van Wyk, 1997). A preliminary survey along a transect from the deep sand-areas west of the lake beds, across the lake beds and up to Female Hill exhibited different vegetation zones (Fig. 4). A true sandveld community (e.g. Sianga and Fynn, 2017) is rather confined to the deep sand-area while vegetation is more diverse on the lake beds, where also the tallest trees flourish, including *Combretum* (bushwillow) and *Adansonia* (baobab) (see Discussion). The vegetation grows under a semi-arid climate, with annual evapotranspiration almost three times higher than precipitation (Fig. 5). A yearly mean of ca. 700 mm rain falls during austral summer while there is little to no precipitation in winter (Fig. 5). The lake depressions can be flooded to shallow depths during heavy rains (Campbell et al., 2010; Fig. A.1). Perennial water is scarce at Tsodilo nowadays and only one site ("Python Spring") is commonly known (Campbell et al., 2010) while other sources do exist but are secret (personal communication with Xontae Xhao, headman of local San).
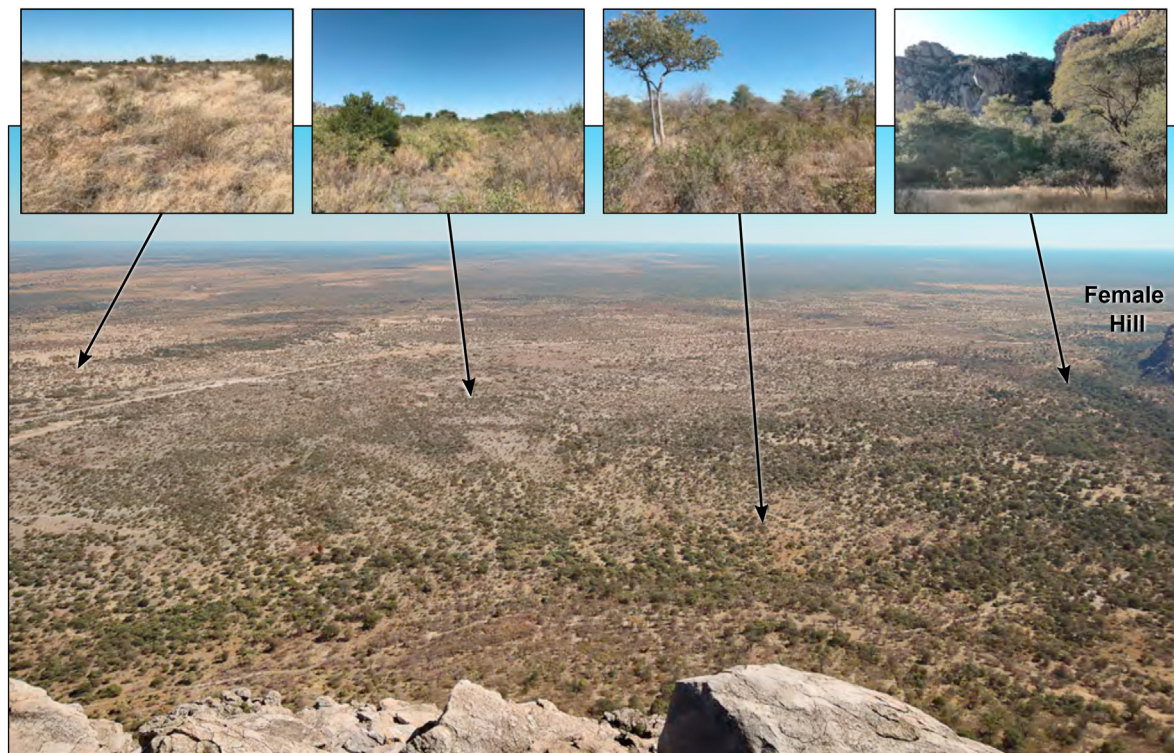
Fig. 4. View from Male Hill to the northwest, across the palaeolake beds. Vegetation types are exemplified.
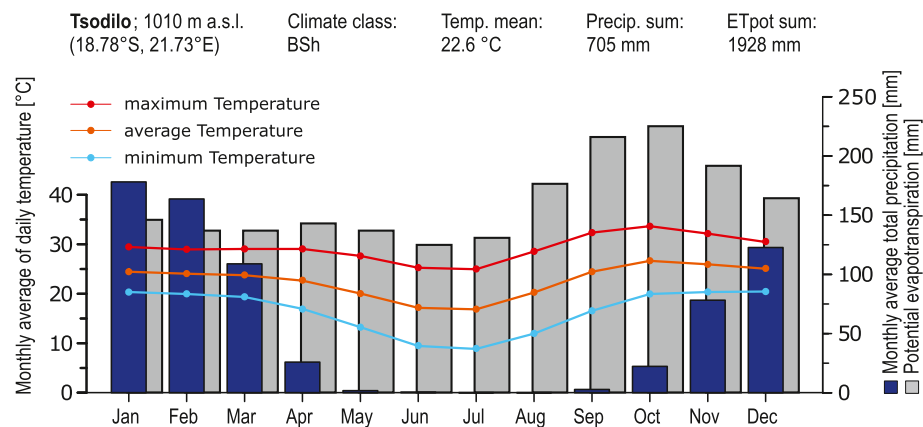

Fig. 5. Climate chart (AD 1981–2010) for Tsodilo. Precipitation and temperature values derived from the ERA5 reanalysis dataset (Copernicus Climate Change Service, 2019). Evapotranspiration values calculated with ETo calculator (FAO, 2012).

3. Material and methods

3.1. Morphometric satellite data analysis

3.1.1. TanDEM-X and Landsat data

The satellite data used for the geomorphological mapping was of two types: (1) a high-resolution digital elevation model (DEM) and (2) Landsat multispectral and multitemporal imagery. The high-resolution elevation data from the TanDEM-X mission (TerraSAR-X add-on for Digital Elevation Measurement; Schulze et al., 2008; Rizzoli et al., 2017) was supplied in 2017 by the DLR (German Aerospace Centre). The elevation data for the studied basin area spans three overlapping source scenes of the TanDEM-X DEM, recorded on 2011-May-26 and 2012-Aug-08, and thus resulting in 2–3 coverages with a spatial resolution of 12×12 m. The height error for the DEM is annotated in the respective TanDEM-X HEM (height error map) with a maximum of about 1 m.

Landsat data from missions 5, 7 and 8 were downloaded from the USGS EarthExplorer website (Table A.3). Only datasets with no cloud cover and no bush fire influence (checked with MODIS data – MOD14A2 from EarthExplorer) were chosen, primarily covering the same period as TanDEM-X data (May 2011, August 2012). Due to a failure of Landsat 7's Scan Line Corrector, the raster data include black stripes with missing data, and thus datasets from other years (2008–2018) but for the same months were added. Additionally, data covering the periods of field campaigns (August 2015, August 2017, June 2018) were acquired, particularly for direct comparison with ground observations of the vegetation. Datasets with best coverage for one whole year (2016) were chosen to retrace seasonal changes of the landscape.

3.1.2. TanDEM-X DEM noise reduction

The elevations in the TanDEM-X DEM are defined in terms of the reflective surface of X-Band interferometric SAR (Synthetic Aperture

Radar) returns. As for short wavelengths (X-band: ~3 cm; DLR, 2009) the penetration of vegetation cover is limited, the backscattered signals originate from within the vegetation cover. Therefore, shrubs and trees are included in the elevation model. The measured vegetation height is affected by SAR inherent effects, as the elevation of the scattering centre depends on the vegetation density, shape and wetness (Fig. A.2; Izzawati et al., 2006; Schumann and Moller, 2015; Tanase et al., 2015). Drier and sparser vegetation cover allows deeper penetration than a dense and moist, placing the scattering centre closer to the ground (Perko et al., 2011; Weydahl et al., 2007; Rizzoli et al., 2017). Vegetation cover may produce a pronounced zigzag-pattern along a TanDEM-X elevation transect, which can clearly be demonstrated in comparison with DGPS data (Fig. A.4). In order to reduce such noise in the TanDEM-X DEM, six different filters were tested: (i) inverse discrete wavelet transformation (IDWT; Kalbermatten et al., 2012), (ii) the geomorphological filters erode (min) and (iii) dilate (max) (Pipaud et al., 2015) as well as (iv) a mean filter, (v) a filter using the Fill Tool (Spatial Analyst Tools) in ArcGIS (ESRI, 2018) on the inverted TanDEM-X DEM and (vi) the low pass filter using the Filter Tool (Spatial Analyst Tools) in ArcGIS. IDWT filters were applied using the Wavelet toolbox from MATLAB (The MathWorks Inc. 2015a, b) whereas the min, max and mean filters were applied with R (R Core Team, 2019b).

Filters that improved correlation with the DGPS profiles were the following: mean filter with a rectangle of 3x3 or 5x5 pixels, lowpass filter and fill filter with 1 m (Table A.5). In areas with dense shrub and tree cover, the filtered data still deviate significantly from DGPS elevations e.g. along the northernmost part of T1 (Fig. A.4). Apart from the fill filter, the application of filters resulted in a decreased spatial resolution. As most of the study area is shrubby grassland, which produces relatively low elevation errors (Fig. A.4; Wessel et al., 2018), we decided to use the original TanDEM-X elevations, locally cross-correlated with DGPS data.

3.1.3. Geomorphological mapping

Three different approaches were combined for the geomorphological mapping: (1) Edge enhancement by a discrete wavelet transform (DWT) filtering procedure (Kalbermatten et al., 2012) for outlining topographic discontinuity that may be related to geomorphological features. The DWT is used to extract these discontinuities of the elevation data, which are then quantified and highlighted in terms of detail coefficients, i.e. scaling coefficients of the DWT (Doglioni and Simeone, 2014). The detail coefficients are mapped and analysed, whereby sudden variations of the coefficients are related to slope variations and discontinuities of the DEM and thus enable the delineation and identification of characteristic landforms (Doglioni and Simeone, 2014). Iteratively applying DWT, a multilevel decomposition of a topographic profile, was helpful for separating large-scale features from local features. This transformation was applied on the TanDEM-X DEM using the Wavelet toolbox in MAT-LAB (The MathWorks, 2015a, b). In a first step, all wavelet functions available in the toolbox were grouped after similarity of shape. To cover all sorts of shape, at least one wavelet of each group was chosen for the analysis, resulting in 19 different wavelets. After the filtering procedure, linear structures visible in the detail coefficients of different levels from each wavelet transformation (Fig. A.5A) were mapped in ArcGIS (ESRI, 2018). Only the details of levels 1–4 were analysed because higher levels gave no additional information.

(2) The application of the TopHat-Transform function allowed the extraction of ridges and valleys (Rodriguez et al., 2002). The white-TopHat function hereby returns the difference between the original image, here the TanDEM-X DEM, and its opening (erosion followed by a dilation) and thus extracts only the peaks with a specified radius, while the blackTopHat function subtracts the original image from its closing (dilation followed by an erosion) and thus retains the valleys with the specific radius (Rodriguez et al., 2002). These morphological operations were performed on the TanDEM-X DEM using the functions whiteTopHat and blackTopHat from the R-package EBImage (Pau et al., 2010; Olés et al., 2018) with the kernel shape set as 'disc' of different radii (5, 9, 11,

15, 19, 23 and 27 px). Again, the linear structures in the resulting images (Fig. A.5B) were mapped in ArcGIS (ESRI, 2018).

(3) Enhancement of the multispectral Landsat images (Fig. A.5C) enabled us to identify hydrologically related geomorphologic entities (see Imbroane et al., 2007). This approach uses various band combinations, band ratios and principal components analysis (PCA) of the bands from each scene. In arid and semi-arid environments, three band colour composites such as RGB images can provide excellent lithologic discrimination (Imbroane et al., 2007). False colour composite imagery e.g. has been proved useful to provide further information on palae-ohydrology as it indicates compositional differences of sediments (e.g. Schuster et al., 2005; Drake et al., 2008; Breeze et al., 2015). Image processing, such as band ratios, can reveal information about the chemical composition of rocks and minerals on the Earth's surface if not completely covered by dense vegetation (Harding and Forrest, 1989; Okada et al., 1993; Imbroane et al., 2007). As the reflectance properties of rock-forming minerals are a function of chemical composition and crystal structure, many minerals have distinctive spectral absorption properties (Hunt, 1980; Goetz et al., 1985; Fig. A.5C). Ferric oxides, for example, have characteristic absorption features in the visible (380–800 nm) and near-infrared region (800–1100 nm), while various phyllosilicates, carbonates and sulphates show their spectral features in the short-wave infrared region (1100–2500 nm) (Okada et al., 1993; Sabins, 1999; Percival et al., 2014). Thus, e.g. for Landsat 5, the ratio of bands 5/7 is expected to be high for clay minerals, because their reflectance is high in band 5 and relatively low in band 7 (Yazdi et al., 2013). A ratio of bands 5/4 enhances areas containing rocks which are rich in ferrous iron (Imbroane et al., 2007) and ratios of bands 3/1 and bands 3/4 are high for iron oxide minerals (Yazdi et al., 2013). Combining the band ratio images to colour composites (colour-ratio-composite images) allows the distinguishing of similar depositional environments. PCA reduces dimensionality while highlighting the information in the whole band spectrum. For Landsat 5 and 7, only the six reflective bands 1–5 and 7 were evaluated together. For Landsat 8, bands 1–7 were used as input for the PCA accordingly. The analyses were done in R (R Core Team, 2019b) and ArcGIS (ESRI, 2018). Detected zones and structures in the resulting images were mapped in ArcGIS. Finally, only those zones and structures that were found in the majority of the analysed TanDEM-X and Landsat images were accepted. A classification of the detected zones and structures to different landforms was done based on conventional photo-interpretation keys (Loelkes, 1983) such as size, pattern, shape, context and relative positioning of the structures and was complemented with a visual interpretation of aerial imagery from the World Imagery layer of ESRI (Fig. A.5D).

Identified former shorelines with a consistency in altitudes were assembled and connected based on TanDEM-X elevations to obtain continuous structures. Lake level heights were derived by filling the basin in ArcGIS (ESRI, 2018) until the respective shorelines were reached. Further lake morphometry metrics were calculated in R (R Core Team, 2019b) using the package lakemorpho (Hollister and Stachelek, 2017; Hollister, 2018), under the simplifying assumption that the former basin morphology was similar to today. The metrics are thus approximated.

3.2. Geophysical measurements

A geophysical survey was carried out in August 2015 along the northern part of the DGPS transect T0, in NNW–SSE orientation through the lake depression (Fig. 6). A total of 2.85 km of seismic refraction data and 12 km of ground penetrating radar (GPR) were acquired along the same profile line. However, for this study only the northern GPR radar-gram (2.6 km) that coincides with the seismic refraction profile has been processed. Both methods use the principle of wave propagation for subsurface imaging. GPR measures traveltimes of electromagnetic waves that are reflected at contrasts of dielectric permittivity. During refraction seismic surveys the measured traveltimes of direct and critically refracted waves depend on the elastic properties of the subsurface materials. Both
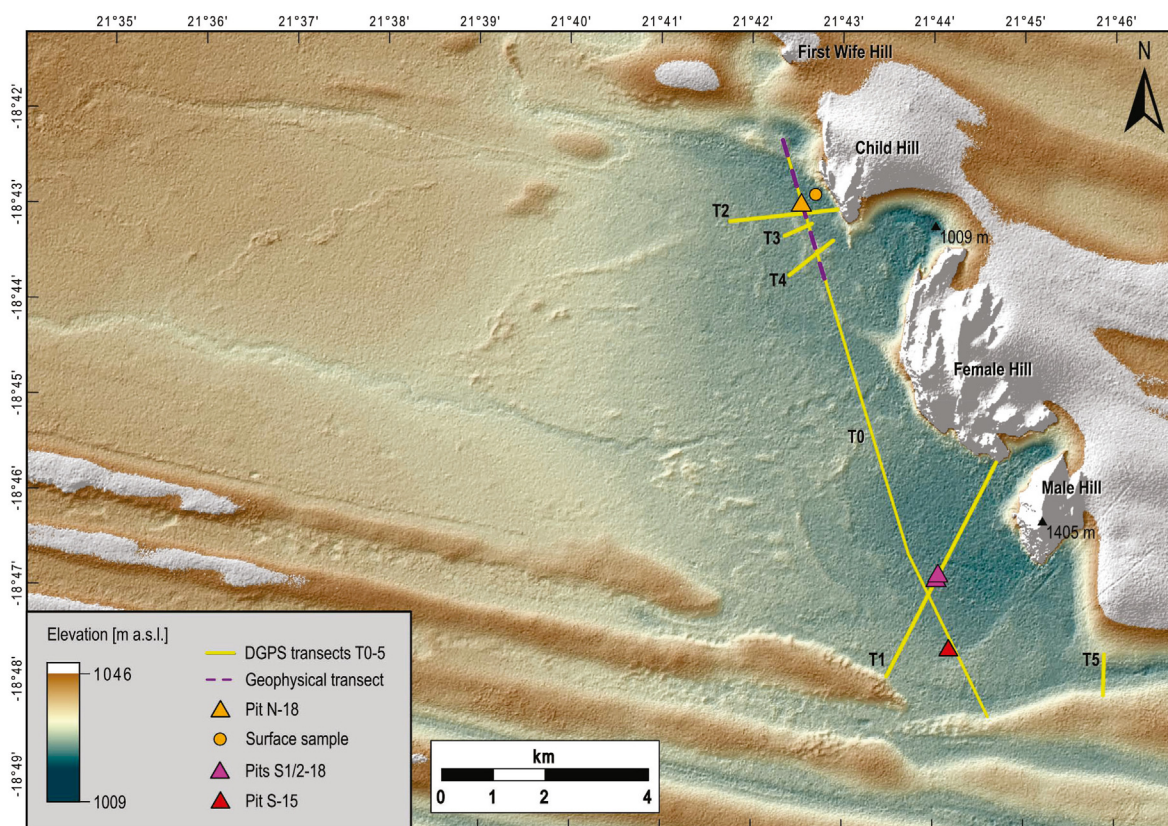
Fig. 6. TanDEM-X DEM showing DPGS and geophysical transects and sediment pits.

data sets are combined aiming to enhance the reliability of data interpretation.

The GPR data were acquired using a MALA GPR system set up. Electric pulses were generated with a 30 MHz rough terrain antenna. These relatively low frequency signals can reach larger depths but at the expense of resolution. Electromagnetic pulses were generated every 10 cm along the 2596 m long profile and recorded with a second antenna at constant distance to the source antenna. The data processing was performed using the processing software ReflexW (Sandmeier, 2017). In a first step, the data were pre-processed. This included high-pass filtering to eliminate low-frequency noise produced by the recording system, static corrections to account for time delays of first arrivals, manual gain in order to compensate for amplitude decay with time and depth, and a background removal filter. Traces were stacked at intervals of three traces in order to amplify the signal. To convert the radargram from time to depth domain, the velocity of the average subsurface electromagnetic waves was estimated using the method of hyperbolic fitting (Cassidy, 2009). Afterwards, Kirchhoff migration (Schneider, 1978) was performed to convert the reflection signals from time domain to its spatial position in the subsurface (Cassidy, 2009).

The seismic refraction soundings were performed using a DMT® Summit II Plus seismic system. A total of 41 geophones (10 Hz, vertical type) were arranged in a split-spread geometry with a geophone spacing of 7.5 m (= 300 m spread). The source was initially located at the northern edge of the spread and moved 30 m after each of the first 6 shots until it was located at the middle of the profile, then the whole spread was moved 30 m after each shot. Seismic signals were produced as a series of pulses, according to a specific pre-programmed sequence by a Bosch Vibrometric VIBSIST-50 as surface seismic source. A total of 91 shots was performed to cover the profile of 2850 m length. Analyses of the resulting 91 single-shot sections were done with ReflexW (Sandmeier, 2017). For the model (Fig. 9), the southernmost 150 m were not included, resulting in 2.7 km distance. The processing sequence included

(1) bandpass Butterworth filter (Butterworth, 1930; Acharya et al., 2014), (2) automatic gain control (AGC), (2) first-arrival picking, (3) traveltime analysis, (4) wavefront inversion, and (5) seismic tomography. For filtering, a bandpass Butterworth filter (Butterworth, 1930; Acharya et al., 2014) was selected between 25 Hz and 80 Hz. An automatic gain control with a time window of 400 ms was applied to enhance weak signals. The picking of first arrivals was done manually. Each pick was accounted to the arrivals of direct and critically refracted waves. Based on the arrival times of each wave type, wavefront inversion gives a model of layer thicknesses and layer velocities. The tomography uses this model as starting model to invert for further lateral velocity changes.

3.3. Differential global positioning system (DGPS) elevation measurements

The DGPS-survey was used to obtain accurate elevation data of selected transects including sample sites and as ground control for remote sensing data. In total, 6 transects (T0–T5 in Figs. 6 and 10) were measured during field campaigns in August 2015 and June 2018. The data were acquired with a measuring device setup from Leica Geosystems AG, consisting of a Leica Viva CS15 field controller, two Leica Viva GS14 GNSS (Global Navigation Satellite Systems) Receivers (3.75G & UHF Single Frequency Smart Antenna) as base and rover, and an external RTK-Antenna. The measurement distance between two points was approximately 25 or 50 m, depending on changes in the landscape, with a measurement time of 60–90 s and Real-Time Kinematic (RTK) processing. For quality control, the limit for maximum acceptable coordinate quality (CQ) for position and elevation was set to CQ3D(max) = 25 mm. Other measurement information such as the different values for positional measurement precision can be found in the supplements (Table A.4). These GNSS-RTK measurements were done without a known elevation (e.g. trigonometric point) as reference for the DGPS base station. Furthermore, the locations of the base station for the different transects were chosen to be on areas with a low density and low height of

vegetation, to ensure an undisturbed satellite signal. For the 2018-transects, if possible, the base station was additionally located on points of the 2015-transect to allow cross-validation. We did not have the option to calibrate the position of the base station with a trigonometric point, thus absolute DGPS-heights have an uncertainty of 2–3 m (Leica Support, pers. communication April 2020); the uncertainty within a single transect, however, is only a few centimetres. For comparison between the transects as well as between transect and TanDEM-X data, all measured DGPS-heights needed to be corrected. Correction was done based on the TanDEM-X heights by subtracting or adding the height difference between each transect's DGPS base station and the respective TanDEM-X height at this location, or in case of T0 and T3, by applying the height difference between a DGPS point in an area with very low and sparse vegetation and the respective TanDEM-X value for the site (values for corrections in Table A.4). Generally, the locations for the DGPS base station were chosen correspondingly. For such sites with low and sparse vegetation, the absolute TanDEM-X elevation values should not exceed the maximum error of 1 m (Wessel et al., 2018; see paragraph on TanDEM-X and Landsat data).

3.4. Sediment analysis

3.4.1. Sampling and lithological description

Sediment Pit S-15 was dug and sampled in August 2015 and resampled in July 2019. The other three pits were dug and studied in July 2018. The pit locations (Fig. 6; Table A.2) were chosen based on preliminary analysis of the TanDEM-X DEM and the geophysical transects. The pits N-18 and S1-18 were both located on sandy plains sparsely covered by shrubby grassland. S2-18 was dug at the edge of a 2 m deep depression (former water hole) surrounded by trees. Some details for Pit S-15 are published in Wiese et al. (2020). The thoroughly cleaned sections of 0.9–3 m thickness were macroscopically described in terms of sedimentological properties as well as fossil content, sketched (Fig. 11) and photographed. Afterwards, the sections were cleaned again and continuously sampled in 5-cm-steps (deviations in respect to lithological changes) using an angle grinder, except for the top metre of Pit S2-18 and the top 50 cm of Pit N-18, which were sampled in 10-cm-steps. Additionally, a surface sample (TD18-50; Fig. 6) was taken that exhibited gastropod shells in abundance. The individual sample volume was about 1.5–2 L. The classification of sediments is based on observations in the field and refined by carbonate content estimated from LOI (see next paragraph). Limestone is characterised by $\geq$37% $CaCO_3$ and marl by <37%–20% $CaCO_3$. Below 20% $CaCO_3$ the material was classified as quartz sand.

3.4.2. Geochemical and mineral analysis

Measurements were performed at the Laboratory of Physical Geography, Department of Earth Sciences, Freie Universität Berlin. Homogenization of the measured aliquots of the bulk sediment samples was achieved in a continuous vibration disk mill. Organic matter and carbonate content were estimated by loss on ignition (LOI) of 1 g homogenized dried (105 °C) sample material at 550 °C (5 h) and 900 °C (5 h) respectively, following the procedures described by Heiri et al. (2001). LOI residuals (Si-remains) were corrected by CaO subtraction based on LOI_{900} CO_2 estimation, assuming that LOI_{900} is 100% related to calcite. To gain information on the variability of the elemental sediment composition, 2 g of the homogenized dried (105 °C) sample materials were semi-quantitatively measured in sample cups using a portable X-ray fluorescence (pXRF) analyser (Thermo Scientific™ Niton™ XL3t XRF Analyser). Measurements were done in the manufacturer's 'mining mode' for (in-device) fundamental parameter calibration, and four filters were selected with an overall measurement duration of 120 s. Only elements with mean values at least four times larger than the 2σ error of the measurements were used for the analyses. Elements were excluded from further analysis if the proportion of samples with values below the detection limit exceeded 15%. Seven elements (Al, Ca, Fe, K, Si, Sr, Ti)

were selected for further analyses. For comparison to measurements by inductively coupled plasma optical emission spectrometry (ICP-OES), the measurement unit was converted from the initial parts per million (ppm) to milligrams per gram (mg/g).

ICP-OES was conducted with a PerkinElmer Optima 2100 DV instrument after HCl (37%) digestion of 1 g homogenized and dried (105 °C) aliquots to determine the content of selected carbonate and/or sulphate related elements (Ca, Fe, K, Mg, Mn, Na, P, S, Sr).

The mineral composition was analysed by X-ray diffraction performed on homogenized dried (40 °C) samples using a Rigaku Miniflex 600. The 2θ range (3–80°) was analysed in 0.02° steps with a copper Kα X-Ray tube at 15 mA/40 kV. Identification of the minerals was based on Philipps X'Pert Highscore 1.0b software. Identified reflex intensities (counts per second: cps) from each mineral main peak were converted into a relative percentage (% cps) of each mineral with respect to the sum of all identified main reflexes of the bulk sediment (Wünnemann et al., 2010). However, estimations of the mineral compositions must be regarded as semi-quantitative.

3.4.3. Multivariate statistics

As the datasets of LOI, elemental and mineral analyses are considered to be compositional, the problem of spurious correlations and non-normality needed to be treated by log-ratio transformations of the intensities and concentrations (Aitchison, 1982, 1986). Therefore, the values were centred logratio (clr) transformed prior to the statistical analyses using the R-package compositions (van den Boogaart et al., 2020) in R (R Core Team, 2019). To overcome the problem of zero count values in the transformation results (Martín-Fernández et al., 2000), these values were set to the respective smallest value of possible detection, e.g. the minimal detection limit. Subsequently, the datasets were made comparable by standardization using a z-transformation. For exploration of the relative correlations and interdependencies between individual elements, PCA was used on the geochemical data. The PCA enables to generate proxies related to hydrological changes and to identify system variables (e.g. Hartmann and Wünnemann, 2009). As ratios of element intensities are considered to be useful for correlation and advantageous compared to the intensities of single elements (e.g. Vlag et al., 2004; Croudace et al., 2006; Richter et al., 2006; Weltje and Tjallingii, 2008), the PCA was also used to extract descriptive ratios of the geochemical data according to the identified system variables. The element ratios were solely built of elements measured with the same method for having a conclusive statement. As ratios are insensitive to dilution effects from the unit-sum constraint (Weltje and Tjallingii, 2008), the geochemical ratios were calculated from the non-transformed values converted in mg/g molar weights and the mineral ratios from the % cps values.

3.5. Radiocarbon dating

Fossil shells of aquatic gastropods were carefully extracted with a pneumatic engraving pen from selected samples of each pit. Shell fragments that could be clearly assigned to the genera *Bulinus* or *Radix* were first cleaned using needle and brush and then in an ultrasonic bath. Four shell samples were ^{14}C-AMS-dated at Beta Analytic Radiocarbon Dating Laboratory in Miami (Beta), USA, and three samples at Leibniz-Laboratory for Radiometric Dating and Stable Isotope Research in Kiel (KIA), Germany (Table 2). As pre-treatment method, (shell) acid etch was used for the four Beta-samples, while for the three KIA-samples no pre-treatment was done due to the small amount of available sample material. The radiocarbon ages [^{14}C yr BP] were converted into calendar ages [cal yr BP] by calibration with Calib 8.1 (Stuiver and Reimer, 1993, 2020), using the southern hemisphere calibration curve SHCAL20 (Hogg et al., 2020). Additionally, given point estimates were calculated using the mode, i.e. the maximum of the probability distribution of a calibrated ^{14}C-date as proposed by Michczyński (2007); in case of more than one age range, a weighted mode was calculated. No reservoir offset was applied, following Riedel et al. (2014).

Table 1

Hydrological characteristics of the four identified lake phases. Lake levels were derived by filling the modern shape of the lake depressions in ArcGIS until the respective shorelines were reached. Other metrics were calculated using the R package lakemorpho (Hollister and Stachelek, 2017; Hollister, 2018).

Palaeolake phase	Lake level	Max. depth	Surface area	Water volume
	[m a.s.l]	[m]	[km^2]	[10^{6}m^3]
P1	1025.0	16.0	70.6	25.1
P2	1019.5	10.5	40.3	13.2
P3	1018.0	9.0	27.6	8.6
P4n (northern sub-basin)	1017.0	8.0	4.9	1.5
P4s (southern sub-basin)	1017.0	6.0	10.6	3.9
drainage area			1756.0	

Table 2

Radiocarbon ages of *Bulinus* and *Radix* shell fragments from the studied palae-olake sediments. * = Wiese et al. (2020). Conventional radiocarbon years [^{14}C yr BP] were converted into calendar years [cal yr BP] by calibration with CALIB 8.1 (Stuiver and Reimer, 1993, 2020), using the southern hemisphere calibration curve SHCAL20 (Hogg et al., 2020). The calibrated dates are given as a range or ranges with the associated probability. Point estimates for the calibrated ages were calculated using the probability distribution mode as proposed by Michc-zyński (2007).

Lab-ID	Sample-ID	Depth	Radiocarbon age ± 1σ	Calibrated age (2σ range)
		[cm]	[^{14}C yr BP]	[cal. ka BP]
Beta-511707	TD18-50	0–10	23300 ± 80	27.4 (27.3–27.7)
Beta-511706	Pit N-18	0–10	38990 ± 380	42.6 (42.3–42.9)
Beta-511705	Pit N-18	140–145	>43500	>46.6
KIA-53512	Pit S2-18	125–130	38100 ± 1300	42.3 (40.5–44.1)
KIA-53510	Pit S1-18	15–20	33300 ± 800	37.7 (36.2–39.8)
Beta-511704	Pit S1-18	35–40	>43500	>46.6
KIA-53511	Pit S1-18	85–90	35200 ± 950	37.8 (37.8–38.0) (1%) 40.3 (38.0–41.9) (99%)
Beta-421941	Pit S-15*	40–45	15540 ± 60	18.8 (18.7–18.9)
Beta-421942	Pit S-15*	90–95	16930 ± 60	20.4 (20.3–20.6)
Beta-421944	Pit S-15*	95–100	35380 ± 360	40.6 (39.7–41.1)
Beta-421940	Pit S-15*	95–100	37830 ± 500	42.2 (41.6–42.6)
Beta-421943	Pit S-15*	125–130	39350 ± 470	42.8 (42.3–43.4)

4. Results

4.1. TanDEM-X and Landsat based geomorphology

The drainage basin (Fig. 2b) extends to about 120 km west of the Tsodilo Hills, has a maximum N–S-extension of 19 km and spans ca. 1750 km^2. The major palaeolake-related results are compiled in Fig. 7. A northern lake depression between Child and Female Hills and a southern depression south of Female Hill can be differentiated. A linear SW-trending structure roughly paralleling the northern heritage site fence (Fig. 7B) represents the only potential fault we could identify (see Discussion). In relation to the lake depressions, four shoreline systems could be identified (see Material and methods section) and are termed as palaeolake phases P1–P4. P1 levelled at an elevation of ca. 1025 m a.s.l. and covered about 70 km^2. The P2-shoreline is about 5–6 m lower than the P1-shoreline and formed at about 1019.5 m a.s.l., while P3 levelled at

1018 m a.s.l. and P4 at 1017 m a.s.l., subdivided into P4 south and P4 north. Calculation of lake areas, water depths and volumes are listed in Table 1. P1 and P2 eroded linear dunes framing the lake basin in the south and dunes in the north, which had formed west of the corridor between Child and First Wife Hills. The western shoreline of P1 cannot unambiguously be identified but follows tentatively the landforms between the terminal southern and northern erosional features. Five major, partly interconnected palaeo-channels were identified, which are aligned from west to east in direction to the lake basin (Fig. 7). The inter-connecting SW–NE channels are less pronounced than the WSW–ESE-channels and partly appear as positive relief. The central channel terminates between the northern and southern lake depressions where the P3-shoreline is concave for about 3 km (Fig. 7). A channel, about 2 km south of Male Hill, is tracked to the Okavango Panhandle (Fig. 8). The channel is approximately 56 km long and slumps from ca. 1015 m a.s.l. (Fig. 8) at its western terminus to ca. 986 m a.s.l. at its eastern terminus. An asymmetric delta, which is about 10 km wide, corresponds to this palaeo-channel (Fig. 8).

4.2. Geophysically constrained subsurface structures

4.2.1. Seismic refraction

The generated tomographic velocity–depth model reaches a maximum depth of ca. 38 m, locally only around 20 m. *P* wave velocities range from ca. 200–2100 m/s (Fig. 9). We are aware that the behaviour of the *P* wave velocity does not only depend on the rock type (e.g. Kearey et al., 2002) but on many lithological properties such as porosity, cracks, density or water saturation (e.g. Kearey et al., 2002; Karaman and Yeken, 2008; Bailly et al., 2019). Velocities measured along the transect roughly provide a spectrum from dry sand to lithified sedimentary rocks (Kearey et al., 2002). A detailed analysis of the data is not in the scope of this paper but certain cross-correlations with surface structures and lithological data from our pits and from the literature (see Discussion). Generally, *P* wave velocity increases with depth, and tentatively, three main velocity layers can be derived (see Material and methods; Fig. 9): The basic layer (violet to red) terminates at ca. 25 m (32–20 m) depth. The thickness of this layer remains unknown. The velocity values of 2100–1200 m/s possibly indicate compact sedimentary rocks (Kearey et al., 2002; see Discussion). The basic layer is relatively homogeneous but horizontal velocity differences are notable, e.g. between the 400–900 m and the 2000–2300 m section of the profile.

The middle layer (pink to green) comprises velocities of 1200–500 m/s and ranges from 8 to 28 m in thickness. The interface between the basic and the middle layer produced strong refraction signals that are clearly visible in nearly each of the seismic sections. This strong velocity contrast indicates a prominent change to less compact or less water-saturated lithologies (Kearey et al., 2002). The middle layer expires around 10 m depth, with significant differences between profile sections. In the northernmost ca. 300 m, e.g., the middle layer reaches 4 m depth, in the middle section (around 1300–1500 m distance) it is close to the surface, while it terminates in around 15 m depth in the southern section. The horizontal velocity variations, particularly in the southern section (from 1400 m distance), exhibit compositional differences. These are likely related to a higher degree of weathering and fracturing (Barton, 2006), or to uncertainties in traveltime picking as the headwave from this layer boundary is hardly visible in the data. A dipping refractor at the interface of the middle and top layer at around 400 m distance (Fig. 9) is noteworthy.

The velocities of the top layer (blue-green to dark blue) range from 500 to 200 m/s which is commonly considered to indicate dry sand (e.g. Kearey et al., 2002). The thickness varies between ca. 1 and 15 m. The top layer exhibits contrasting velocities with ca. 400 m/s velocity (bright blue) on the one hand and ca. 200–300 m/s (dark blue) on the other hand. From distance 1500 m on, a hinge-like pattern between ca. 12 m deep dark-blue areas and the bright blue zones is noticeable.
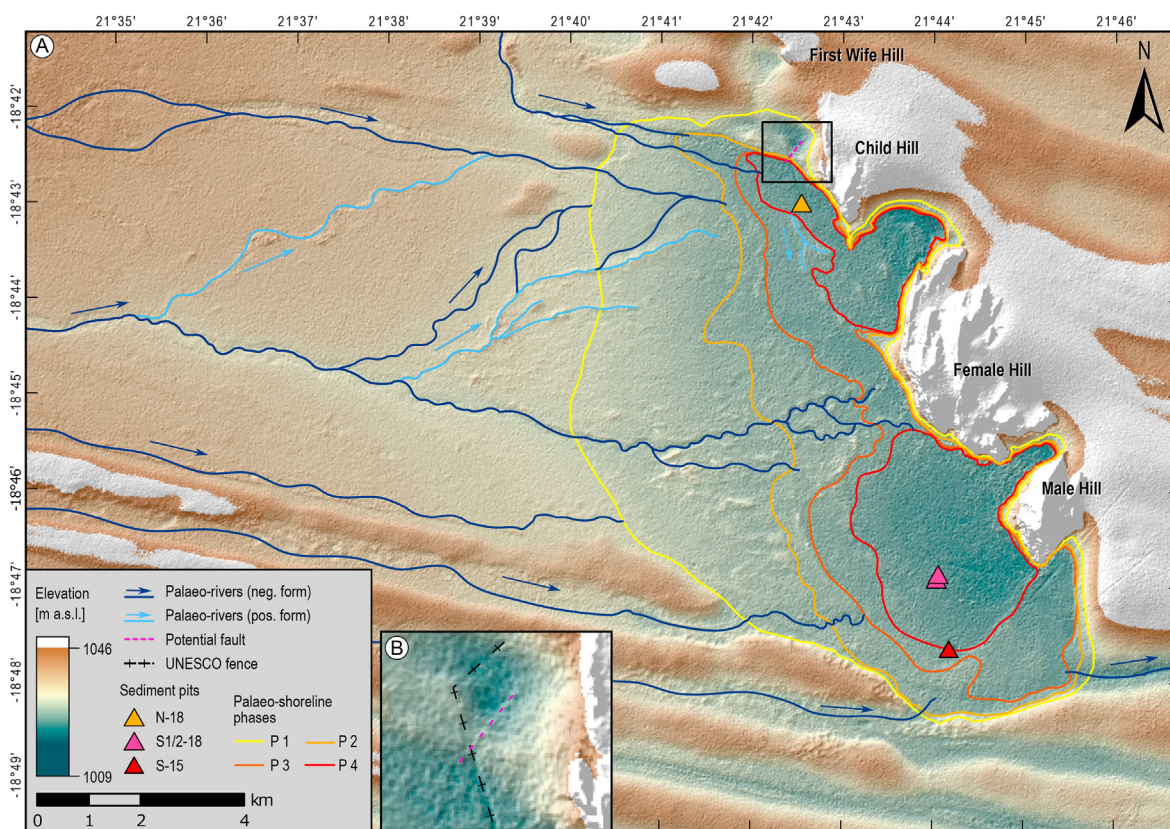
Fig. 7. A. TanDEM-X DEM exhibiting major palaeo-shorelines and -rivers. B. Magnification of the area with a supposed tectonic fault.
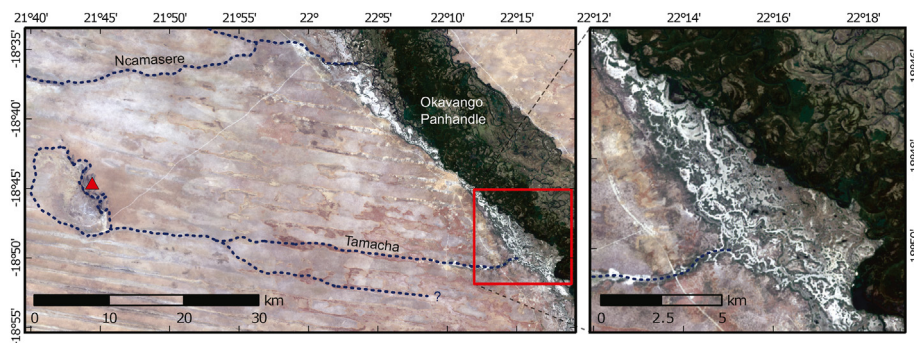

Fig. 8. Landsat image with the course of the former Palaeolake Tsodilo outflow sketched. The outflow created the Tamacha River, which formed a pronounced delta in the Okavango Panhandle. The red triangle indicates the position of the Female Hill and the dashed line passing it follows the highest palaeo-shoreline we could infer.

4.2.2. Ground penetration radar

The GPR data was interpreted by visually identifying sequence boundaries and hyperbolas along the profile, as well as calculating electric parameters to obtain further information from the subsurface (Fig. 9). The velocity for the migration was calculated using the hyperbolas located between 3 and 18 m depth. Hyperbola fitting has given an average velocity of 0.13 m/ns. However, using hyperbola fitting, the velocity estimation was only possible to a depth of 20 m. The dielectric constant was determined to be 5.32, which is in the range of e.g. dry soil, sand, limestone or sandstone (Cassidy, 2009). At the top of the radargram, the continuous black and white 2 m deep banding (Fig. 9) is the result of the air- and groundwave travelling directly above and along the surface interface. These do not represent reflections and negate the ability to distinguish objects in the very shallow subsurface. The yellow ellipses (Fig. 9) likely frame reflections from the surface because an unshielded antenna was used and therefore the electromagnetic field spread in all directions. A high concentration of hyperbolas, creating chaotic reflections, was found at the northern 400–500 m of the transect down to 18 m (Fig. 9). The strong amplitudes in this section might indicate materials with high resistivity that could for example be related to cavities. However, these diffraction hyperbolas could also indicate solid objects in the subsurface. The size of the respective structures would be of around 1 m. A reflection band which is in ca. 4 m depth at 0–400 m distance is continuous along the whole profile but shows a vertical offset of ca. 1.5 m around 400 m distance and is thinning out southwards (Fig. 9, red dashed line). The vertical offset area including greater depths is marked by a rectangle. At ca. 920 m and ca. 1100 m small bow-shaped excursions of the reflection layer can be observed. A larger bow-shaped structure down to 9 m depth is visible from ca. 1600 m to >2600 m (orange dashed line in Fig. 9).

4.3. DGPS ground control

Six DGPS transects (**T0-T5**) were measured (Fig. 10; Table A.4). **T0:**

Seismic refraction tomography

Ground penetration radargram

Combined image
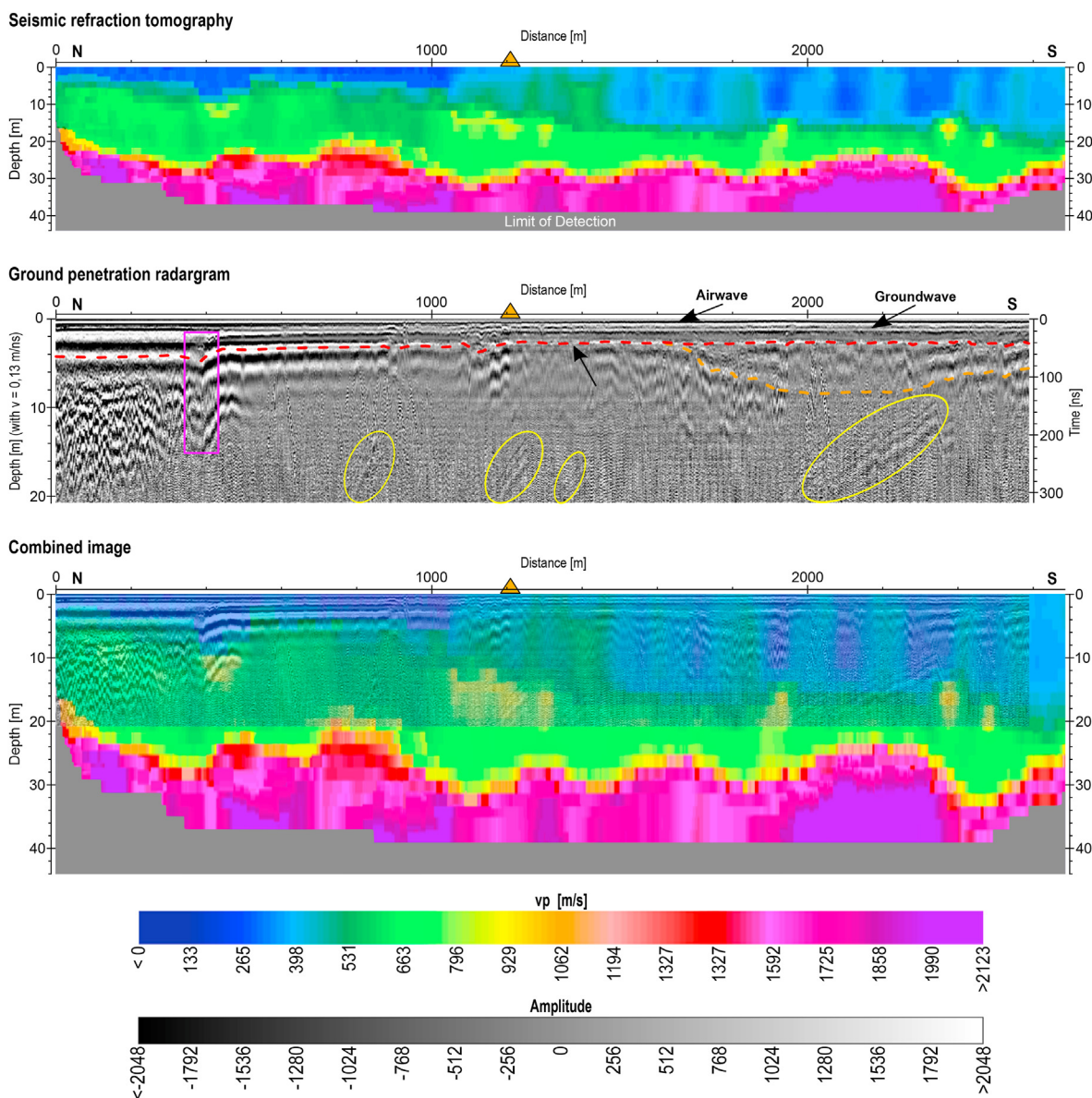
vp [m/s]

Amplitude

Fig. 9. Seismic refraction tomography (top), ground penetration radargram (middle) and combined image (base). Orange triangle indicating the location of Pit N-18 (see Fig. 6). Further information in the text.

Ca. 12 km in NNW–SSE direction across the whole lake basin with an elevation amplitude of 10.2 m; T0 generally shows that a northern and a southern lake depression are separated by an incised ridge at ca. 4.5–7 km; the northern lake depression is more heterogeneous (compare Wiese et al., 2020). **T1**: Ca. 4.7 km in SSW–NNE direction across the southern lake depression with an elevation amplitude of 7.6 m; T1 shows a relatively regular altitudinal decline with the lowest position close to the Female Hill. **T2**: Ca. 2.1 km in W–E direction through the eastern part of the northern lake depression with an elevation amplitude of 5.5 m; T2 generally dips towards the Child Hill and exhibits two ridges at ca. 0.4 km and 1.2 km **T3**: Ca. 0.6 km in WSW–ENE direction within the northern lake depression and with an elevation amplitude of 4 m; the main feature exhibited is a ridge from ca. 0.2 km–0.4 km **T4**: Ca. 1.1 km in SW–NE direction within the northern lake depression and with an elevation amplitude of 5 m; two ridges spaced ca. 0.4 km apart and a lower elevation in the east than in the west are exhibited. **T5**: Ca. 0.8 km in N–S direction across the potential paleolake outflow area with an elevation amplitude of 10 m; the profile is roughly U-shaped; the southern slope shows a terrace-like structure at the base.

4.4. Sediment records

4.4.1. Lithology

In Pit N-18 (Fig. 6), a geological profile (Fig. 11a) from the surface to 190 cm depth exhibits predominantly cemented sand from 190 to 110 cm. From 145 to 140 cm gastropod shells were retrieved. Above this fossil bearing layer calcareous crusts and silcretes are intercalated. From 110 to 45 cm interbedding of marl and cemented sand is marked by silcrete layers. A 30 cm-sequence of light limestone follows. The sequence terminates with carbonate pebbles in a soil matrix in which gastropod shells were found.

The profile of Pit S2-18 (Fig. 6) reached a depth of 220 cm (Fig. 11a). The basic 30 cm are characterized by limestone containing gastropod shells, a soil sequence and marl. This marl and the 35 cm thick limestone sequence above exhibit pockets of soil. Subsequently, a few centimetres of marl underly a sandy sequence containing nodular calcretes. At the transition from that sandy facies to a ca. 1 m thick chernozem-like soil sequence, an accumulation of calcretes and carbonatic pebbles was found, with gastropod shells contained. The profile terminates with
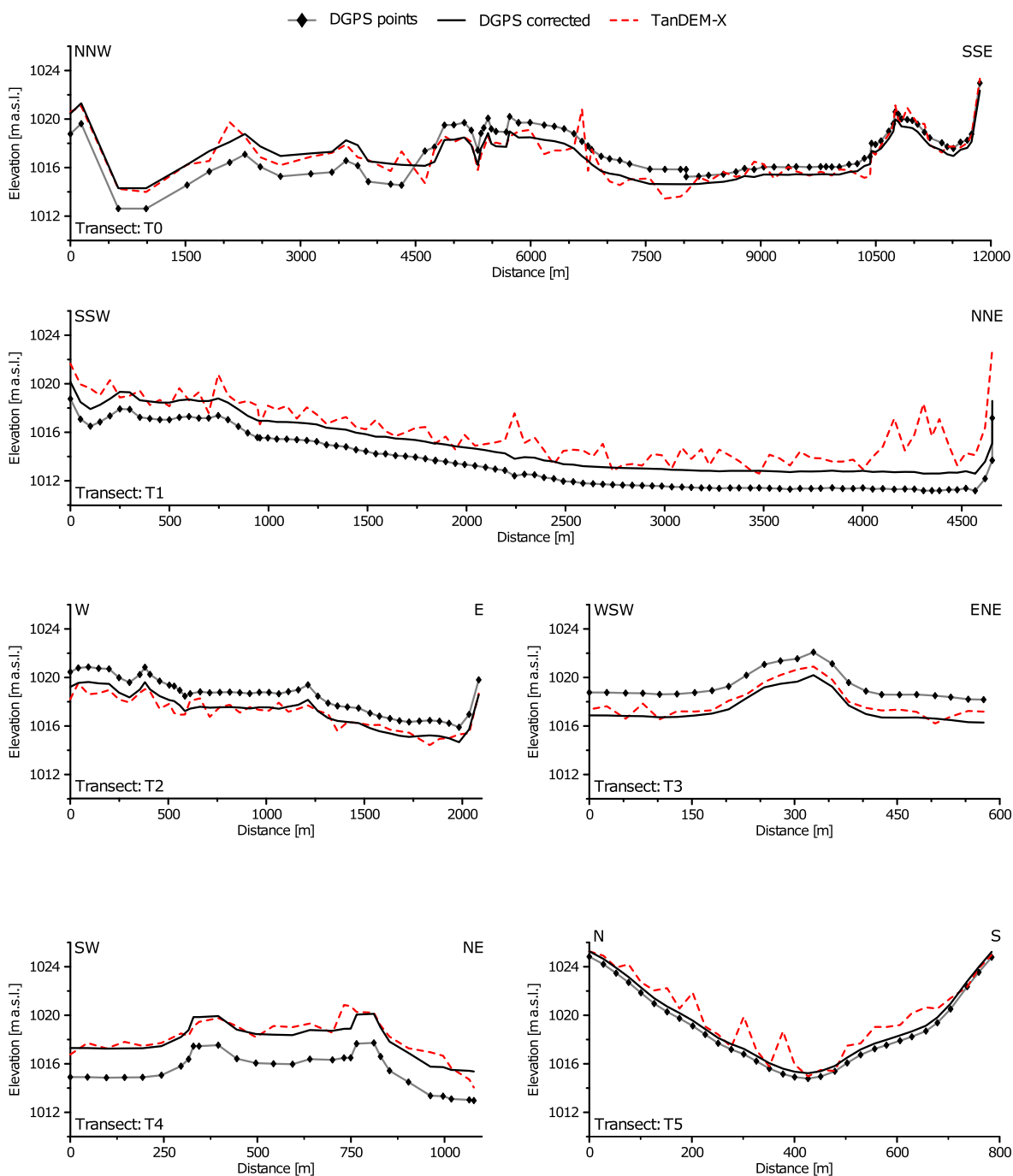
Fig. 10. DGPS-elevation-profiles T0 to T5 (Fig. 6) with corrected and uncorrected values in comparison with TanDEM-X data.

calcrete-rich sand and contemporary soil.

The 90 cm-sediment profile of Pit S1-18 (Figs. 6 and 11a) is characterized by 80 cm of carbonatic facies with a couple of silcrete layers intercalated and gastropod shells relatively abundant. The terminal 10 cm represents soil.

The Pit S-15-record (Fig. 6) covers 295 cm (Fig. 11b). The basic 30 cm are composed of cemented sand, followed by 110 cm-interbedding of marl and light limestone, with two prominent silcrete layers found in the limestone. Subsequently, the facies changes from sand to marl and limestone. This pattern is repeated, with the difference that the second limestone section is much thicker (from ca. 110 to 40 cm) and exhibits a prominent silcretic crust (at ca. 95 cm). Gastropod shells (details in Wiese et al., 2020) were found in abundance from ca. 140 to 40 cm, independent from a sandy, marly or carbonatic facies but in the latter, the

abundance was particularly high. The terminal 40 cm are classified as a soil sequence.

4.4.2. Geochemical and mineralogical composition

In all four pits, eight minerals and mineral groups were identified from X-ray diffraction patterns: quartz, calcite, sepiolite, palygorskite, illite, albite, gypsum and leucite/potassic feldspar. The PCA of the geochemical data was reduced to PC1 and PC2, which account for 70% of the total variance (PC1: 56%; PC2: 14%; Fig. A.6). The variables of Al_{XRF}, Mn_{ICP}, Ca_{XRF}, TIC, Ca_{ICP}, Sr_{XRF}, Sr_{ICP} are highly correlated to each other (group 1) and negatively correlated to the variable group (2) of K_{XRF}, Fe_{ICP}, Ti_{XRF}, Fe_{XRF}, Si_{XRF}, Si_R, K_{ICP} (Fig. A.6). Another group (3) of highly correlated variables is formed by PO_{4-ICP}, Mg_{ICP}, Na_{ICP} and TOC, which are uncorrelated to groups 1 and 2 but negatively correlated to S_{ICP}.
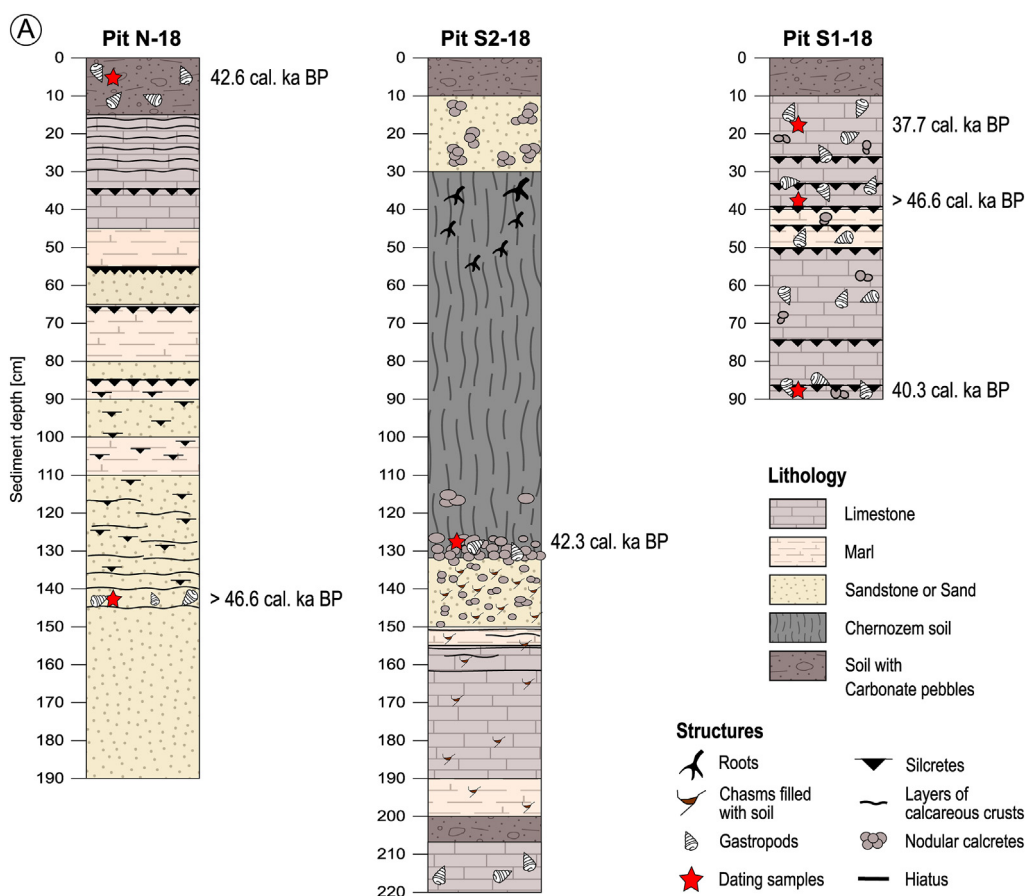
Fig. 11. A. Lithologies and radiocarbon ages of pits N-18, S2-18 and S1-18. B. Lithology and selected geochemical and mineralogical properties for Pit S-15. Radiocarbon ages from Wiese et al. (2020) are marked with red asterisks.

Based on these observations, the ratios Ca/Ti, calcite/quartz, palygorskite/quartz, sepiolite/quartz, Sr/Ca, Mg/Ca and feldspar(sum)/quartz were chosen to infer sedimentological processes and are presented in Figs. 11B and 12 and A.7. The complete data set is compiled in Table A.6.

4.4.3. Chronology

The radiocarbon ages are compiled in Table 2. The Pit S-15-dates are from Wiese et al. (2020; red asterisks in Fig. 11B). Three dates were obtained from Pit S1-18, one from Pit S2-18 and two from Pit N-18 (red asterisks in Fig. 11B). One surface sample (TD18-50) from the northern sub-basin was dated as well. The ages range from 43.4 to 18.7 cal ka BP.

5. Discussion

5.1. Landscape evolution with focus on hydrological settings

The highest of the remote sensing analyses inferred palaeo-shoreline systems (Fig. 7) implies that the maximum extension of Palaeolake Tsodilo was almost twice as large as suggested earlier (Brook, 2010). Based on the modern surface morphology, the lake reached a depth of ca. 16 m in proximity to the Tsodilo Hills and thus was much deeper than previously assumed (e.g. see Thomas et al., 2003). Large areas further to the west, however, are considered shallow and the lacustrine environment was likely interlinked with wetlands. This assumption is extrapolated solely from the surface morphology as the sediment pits were dug in the deeper areas of the lake depressions. The satellite data suggest that during three of the four lake periods an outflow was active which terminated in the Okavango Panhandle (Fig. 8). The bed of this

palaeo-river passes the village of Tamacha (Tamatshaa in Brook, 2010) after which we name it Tamacha River (see also Tamacha Valley in Nash et al., 2006). The delta of the Tamacha River has a size similar to that of the Ncamasere River (Fig. 8), which was reported active in historical times (Robbins et al., 1994) but in more recent times has mainly received inflow from Okavango floods (Nash et al., 1997). The Tamacha River is considered the most likely gateway of ancient people to the Tsodilo Hills. Migrating along rivers makes particularly sense in arid landscapes, and such human behaviour was e.g. suggested in respect of crossing the Sahara during 130–100 ka (Coulthard et al., 2013).

Wiese et al. (2020) identified two Palaeolake Tsodilo highstands which occurred during MIS 3b and LGM, respectively. Based on fossil gastropod communities which indicate littoral habitats under freshwater to oligohaline conditions, an active outflow was concluded (Wiese et al., 2020). Our data substantiate these conclusions. The MIS 3b-lake-highstand lasted from ca. 42.8 to ca. 37.7 cal ka BP. The older age originates from Pit S-15, which is situated in a 1–2 m higher position than the other pits (Table A.2), and thus clearly exhibits the onset of the highstand, while the termination of the lake period is only tentative. As the palaeo-lacustrine record is capped by erosion in the Pit S-15-record, the date of 37.7 cal ka BP comes from a ca. 1 m lower position indicating that the palaeolake was already regressing. Thomas et al. (2003) reconstructed lacustrine conditions during 40–32 ka using surface samples across the southern lake depression (Fig. 3) and suggested a "rather deep" (5–7 m) and permanent lake during ca. 40 ka which is in line with our results, except that we calculate the water depth a few meters deeper (Table 1). Shells from Pit N-18 and Pit S2-18 (Fig. 6) were dated to ca. 43–42 cal ka BP confirming that a continuous freshwater lake spanned from off Child Hill to south of Male Hill. The different lithologies of the
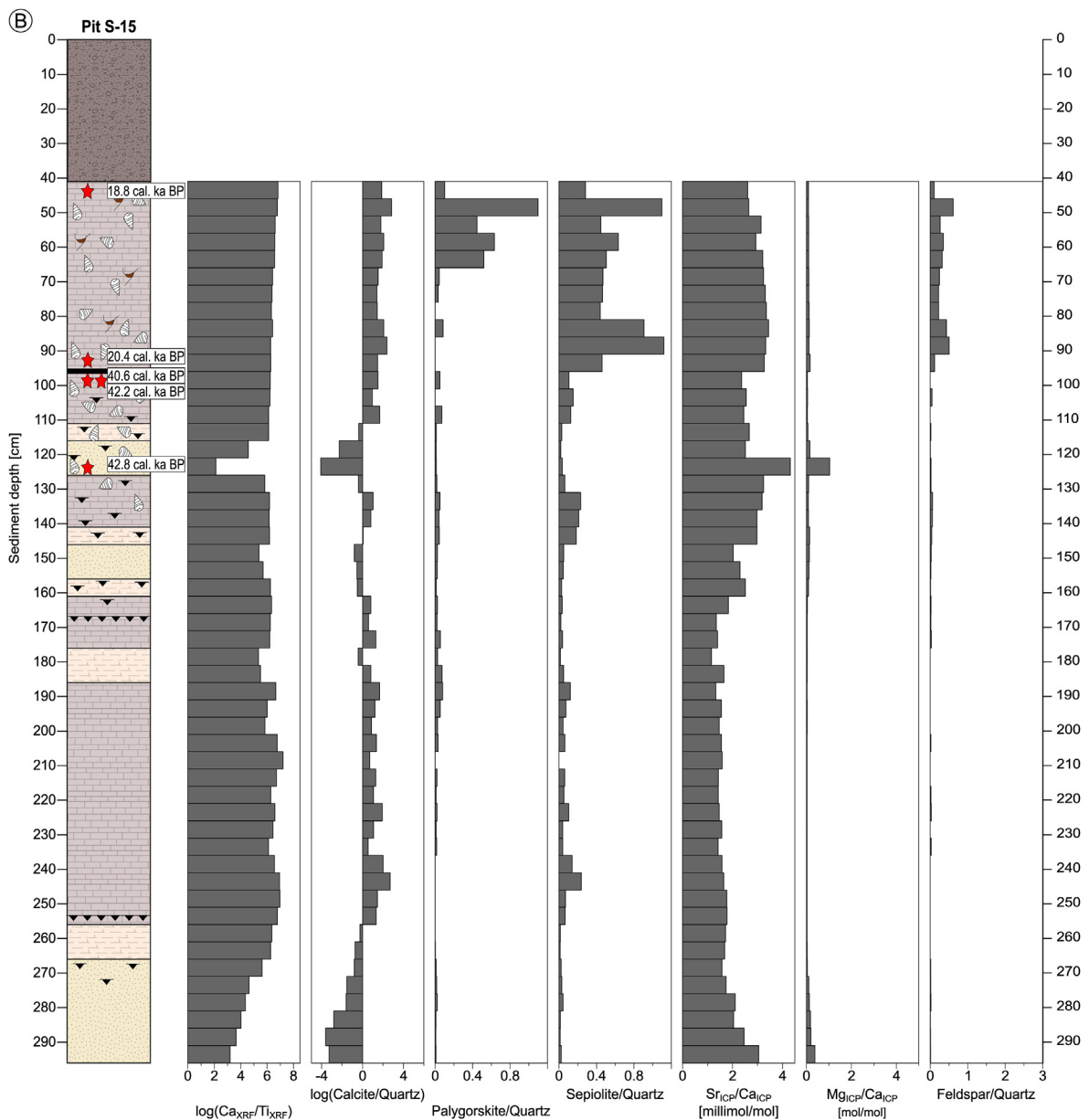
Fig. 11. (*continued*).

pits (Fig. 11) on the one hand reflect contrasts in erosion and soil formation and on the other hand the specific positions regarding fluvial inputs. A PCA of selected elements and chemical compounds indicates strongest differences between Pit N-18 and Pit S-15 (Fig. A.6). Fluvio-lacustrine sedimentation at ca. 43–42 cal ka BP is in phase in pits S-15 and S2-18. In Pit S2-18, the subsequent lacustrine sediments must have been eroded and substituted by a chernozem-like soil, while in Pit S-15 the establishment of full lake conditions is archived and reflected by i) a higher Ca/Ti-ratio, ii) an overturn from allogenic quartz deposition to authigenic calcite precipitation, iii) increased strontium values, which we relate with a stable lacustrine environment, iv) slightly amplified siallitic weathering of the Tsodilo rocks, indicating higher humidity, and v) significantly increased palygorskite and sepiolite precipitation (Fig. 12). Precipitation of palygorskite and sepiolite e.g. occurs preferably under shallow water conditions and pH values from 7.7 to 8.5 (palygorskite) and 8 to 9.5 (sepiolite), respectively (Birsoy, 2002; Galán and Pozo, 2011; Pozo and Calvo, 2018). Our data (Fig. 12, A.7A-C) therefore suggest that the pH varied around 8.5 throughout the lake during MIS 3b. Invading aquatic organisms from the Okavango River,

which migrated via the Tamacha River to eventually reach Palaeolake Tsodilo, must have been able to cope with these slightly higher alkaline conditions. The pH of the Okavango Panhandle and Delta ranges from ca. 6.5 to 9.0 (Mmualefe and Torto, 2011).

The LGM-highstand of Palaeolake Tsodilo is archived in Pit S-15 only (Fig. 12). A major difference to the MIS 3b-lake is that the level was 1–2 m higher. This is mainly inferred from the fossil gastropod community (Wiese et al., 2020). Higher humidity favouring the development of an LGM-lake larger than the MIS 3b-lake is indicated by comparatively stronger siallitic weathering, which on the other hand favours precipitation of palygorskite (Singer, 1979) and thus could explain the relatively high quantities in our LGM-record. Precipitation of palygorskite became high only during the second half of the lake period while sepiolite precipitation increased strongly with the onset of the LGM-lake. The other geochemical proxies are in line (Fig. 12). The age of ca. 27.4 cal ka BP (Table 2) of the surface sample from a lower position of the northern basin demonstrates that a less extended lake existed prior to the LGM-highstand. This corresponds to findings of Thomas et al. (2003).

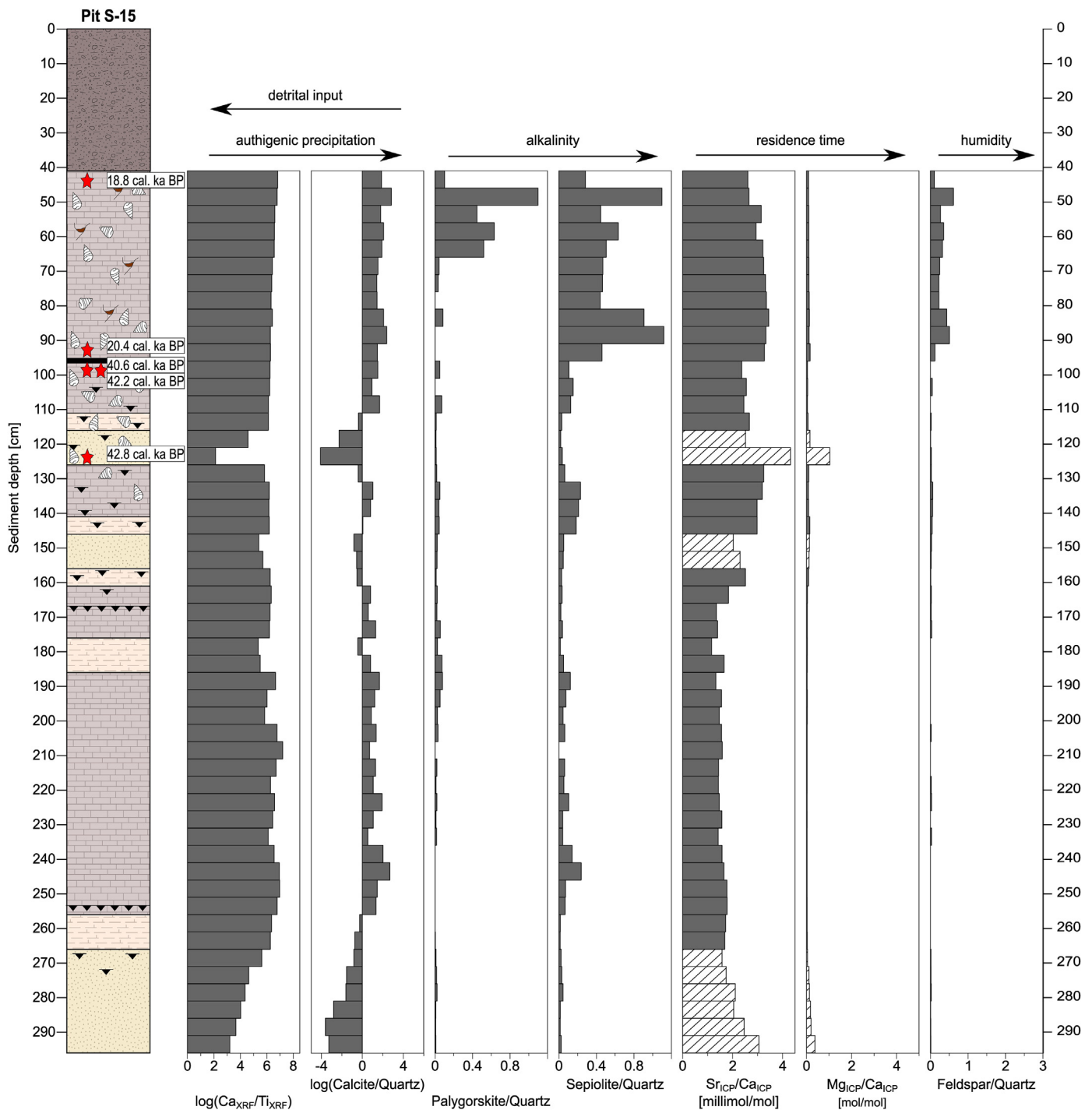The LGM-highstand can be related to Phase 2 of the palaeo-shoreline

Fig. 12. Interpretation of selected geochemical and mineralogical properties of Pit S-15-sediments. Cross-striped bars indicate values not considered for interpretation due to allogenic deposition. Corresponding graphs for other pits are provided in the supplements (Figs. A.7A-C).

systems (Fig. 7). A simulation of the palaeolake and corresponding fluvial systems is shown in Fig. 14B. The MIS 3b-highstand relates to Phase 3 (Fig. 7A) as outlined in Fig. 14C. Phases 1 and 4 could not directly be identified in the records of the sediment pits. The limestone-like, solid carbonatic facies, a meter below the MIS 3b-lake-period in Pit S-15 (Fig. 12), e.g., did not contain any fossil remains of aquatic taxa such as gastropod or ostracod shells or gyrogonites of characean algae. On the other hand, gastropod shells from Pit S1-18 and Pit N-18 were dated to >46.6 cal ka BP. Due to the stratigraphic position in Pit S1-18 (reverse age) and the sandy facies in Pit N-18, we consider both assemblages allochthon. We propose that the shells may originate from the palaeo-

littoral of Phase 1 (Fig. 7) from the higher position of which they were eroded and transported to lower areas. The western shoreline of Phase 1 is difficult to pinpoint because it is largely covered by sand. However, during Phase 1, the linear dunes framing the lake basin in the south and in the north were eroded by the lake and thus the age of the dunes may indicate the maximum age of the highstand. Thomas et al. (2003) luminescence-dated two dunes south of the palaeolake depressions (Fig. 3) to ca. 23–107 ka. Ages increased with sample depth indicating that the upper few metres of the dunes were active until ca. LGM, but the major dune formation is older than 107 ka. Cooke (1980) assumed that the huge E–W-trending linear dune system, extending over hundreds of
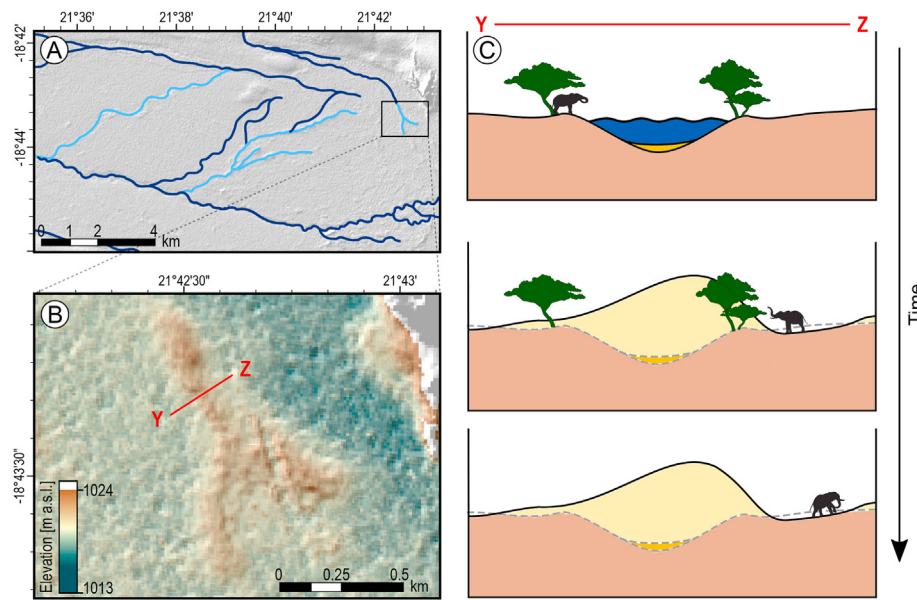
Fig. 13. A. Inverted sections (light blue) of palaeo-river beds with focus on a Y-shaped structure. B. TanDEM-X image of Y-shaped positive form. Red line refers to the position of C. River bed inversion by accumulation.
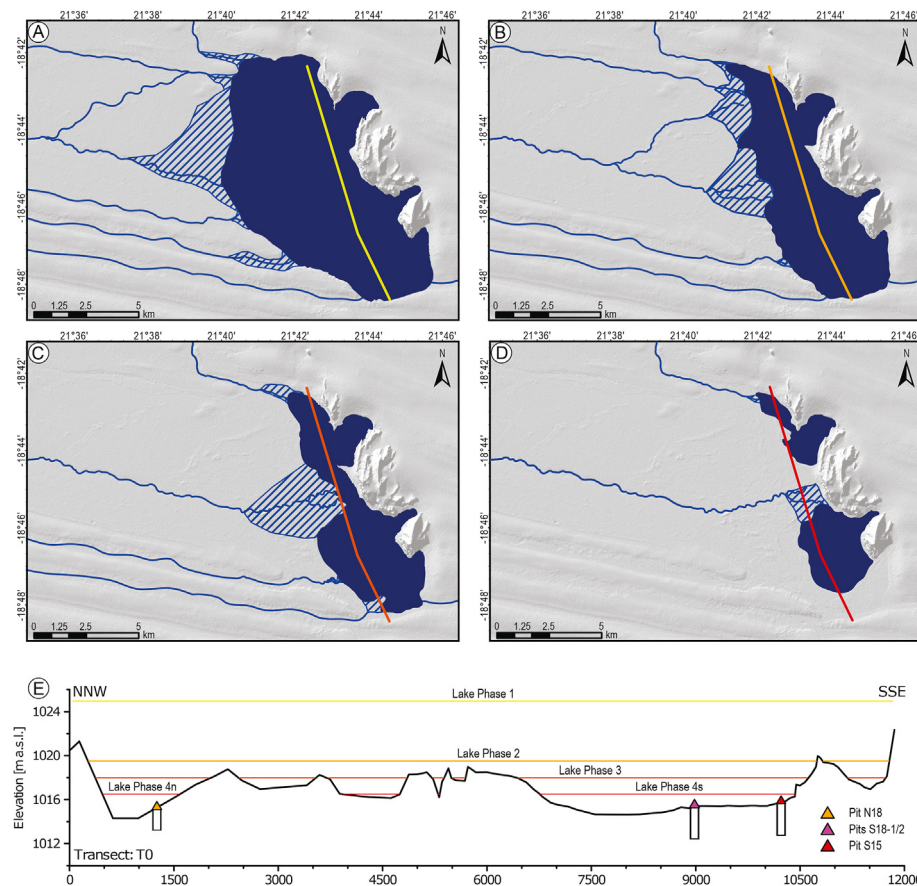

Fig. 14. Simulation of reconstructed fluvio-lacustrine systems. Hatched areas indicate alluvial fan deltas. DGPS transect T0 indicated; different colours referring to Fig. 14E. A. Hydrological setting during ≥100 ka. B. Hydrological setting during LGM. C. Hydrological setting during MIS 3b. D. Hydrological setting during an undetermined period. E. DGPS transect T0 in relation to settings A-D.

kilometres (see e.g. Lancaster, 1981; Chase, 2009), developed during the "late Tertiary" (see also McFarlane and Eckardt, 2007). Jahn et al. (2003) studied a sediment core from Walvis Basin and concluded strong easterlies during 1.5–0.58 Ma while afterwards the amplitude of aeolian input was much lower. We thus tentatively suggest that the formation of the linear dune pattern terminated ca. 600 ka ago. This provides a window of half a million years during which Palaeolake Tsodilo Phase 1 had persisted for an unknown time. Following Robbins et al. (2016) that the

Tsodilo Hills were inhabited by humans since at least 100 ka, an active Tamacha River may have served as a gateway during Phase 1. Schmidt et al. (2017) reconstructed a mega-lake period at ca. 100 ka in the Makgadikgadi Basin and suspected the Okwa River as the major tributary. The catchment of the Okwa River is only 400 km south of the Tsodilo Hills and thus it seems possible that climate settings of the two areas were similar.

The geophysical surveys of the sediments in the northern lake depression allows tentative identification of lake carbonates as well as geological and geomorphological structures (Fig. 9). From observed thick sand layers on the surface and from the excavated sediments of Pit N-18, we interpret the dark blue colour in the seismic refraction tomography to indicate unsolidified sand and the bright blue colour solidified low-density carbonates or alternating deposition of unsolidified sand and solidified low-density carbonates. Down to the limit of detection, the greenish to violet colours indicate increasing solidity and density of sandy to carbonatic sediments. This corresponds roughly with the lithology of a sediment core from the southern lake basin (Linol et al., 2015; location in Fig. 3). Weathering and erosional processes are supposedly indicated by the rugged course of the sediment layers (Fig. 9 top). High concentration of diffraction hyperbolas in the ground penetration radargram (Fig. 9 middle) may hint at karst formation, the local occurrence of which was directly observed in Pit S2-18. The ground penetration radargram exhibits a whitish layer just below the groundwave which levels close to the MIS 3b-carbonates. An exact assignment is not possible, however. The whitish layer in 4 m depth at distance 0 m shows a vertical offset of 1.5 m at 400 m distance, a position which corresponds well with the lineament observed on the surface (Fig. 7). We thus consider a tectonic fault, which, however, had little or no influence on the MIS 3b- and LGM-lake-periods, but possibly on the ≥100 ka-highstand. This tectonic fault trends in the same direction as the major faults of the northern and central Kalahari (Shemang and Molwalefhe, 2011).

The large bow-shaped structure in the radargram, from ca. 1600 m distance (dashed orange line in Fig. 9), corresponds to a Y-shaped positive structure (Fig. 13). The bow-shaped structure represents a former river bed and the Y-structure is considered an inverted part of the fossil river with a bifurcation at the transition to a former alluvial fan delta. The relief inversion was triggered by accumulation of sand, likely under groundwater influence (Fig. 13C). Such positive Y-structures have been described from certain ancient fluvial systems (e.g. Day et al., 2019). Relief inversion also occurred in channels west of the Y-structure (Fig. 13A).

During Phase 4 (Fig. 7), Palaeolake Tsodilo was separated by the progressing central alluvial fan delta into two sub-systems (Fig. 14D). The outflow was most likely not active, leading to a higher salinity under which the gastropod communities, characteristic of the MIS 3b- and LGM-highstands, could not sustain for long. The water was not potable for ancient humans. Three of our sediment pits are within the area which Phase 4 spanned, a clear assignment of the lake stand is not possible, however. Possibly the sediments which were deposited during Phase 4 are not archived because of erosion. Alternatively, it can be assumed that Phase 4 is archived in Pit N-18 within the 45–15 cm sediments and in Pit S2-18 within the 190–155 cm sediments, both sequences older than ca. 43 ka. Interestingly, not this >43 ka-lake period exhibits feldspar influx similarly high as during LGM but the preceding sandy to marly sediment sequence, reflecting the onset of lake formation in Pit N-18. We thus assume that in this case humidity was not particularly high, but comparatively strong influx of feldspar rather derived from pluvial-fluvial resuspension of feldspar-rich pan sediments which do exist in proximity of the First Wife and Child Hills (Fig. 7).

On the one hand, the ancient Tsodilo people lived in a highly dynamic landscape. On the other hand, lake highstands, which lasted a couple of thousand years, occurred at least two times and reflect relatively long periods of environmental stability during which a freshwater Palaeolake Tsodilo had an outflow feeding the Okavango Panhandle. During periods of lower lake levels with higher salinity, such as Phase 4, riverine inflow

was still considerable and thus potable water was abundant. In contrast to the Okavango Panhandle and Delta, the Tsodilo region was tectonically rather calm. This is not only inferred from the single small fault we detected but also suggested by a lack of big boulders in the lake beds near the Tsodilo Hills. Extended dune formation rather occurred before ancient people arrived at the Tsodilos. The age of relief inversion of river bed sections is unknown. However, as some of the fossil rivers with positive relief are within the former lake basins (Fig. 7), we tentatively consider the relief inversions (Fig. 13) younger than 100 ka. Likely, these sand accumulations formed during dry periods when the lake beds were deflated.

5.2. Hunting, fishing and gathering under changing hydrological settings

A changing hydroclimate, with Palaeolake Tsodilo and Tamacha River present or absent, certainly influenced food supply for ancient Tsodilo people. Robbins et al. (2000) compiled a list of fossil mammal and reptile bones excavated at White Paintings Rock Shelter (WPS in Fig. 3, Fig A.11). These remains were generally related to human palaeo-food (Robbins et al., 2000); leopard and hyena, however, probably were not on the menu shale but indicate serious dangers for humans. Brain (1981) entitled his book about cave deposits and early humans "The hunters or the hunted?", questioning the dogma that stone age people could skilfully cope with their dangerous environments. During lake periods, e.g. elephants and lions must have been abundant at Tsodilo and thus the hills did not only provide shelter from weather hazards but also from dangerous animals which are not able to ascend the steep rocks. On the other hand, the hills were ideal watch towers for spotting either such dangerous animals or game. There can be little doubt that WPS was occupied over a hundred thousand years or so (Ivester et al., 2010) but the temporal resolution of sedimentological data (Robbins et al., 2000; Ivester et al., 2010) is too low to demonstrate permanent occupation sensu stricto. Quite some other vertebrates also use rock shelters as homing structures during absence of humans (e.g. Mentzer, 2017). Moreover, an undisturbed character of the WPS deposits is highly questionable. Staurset and Coulson (2014) pointed out that reversed dates (see Robbins et al., 2000) can be best explained by sloping deposits and post-depositional processes. Robbins et al. (2016) admitted large chronological uncertainties but found it feasible to outline general patterns of environmental change. The hunted game included wetland species such as cf. lechwe and cf. reedbuck during periods when fishing was particular important (Robbins et al., 2000).

Along this line, we suggest that radiocarbon- and OSL-dates (Feathers, 1997; Robbins et al., 2000, 2016 with improved ages based on Ivester et al., 2010) of the "Lower Fish" and "Upper Fish" deposits are uncertain enough that the MIS 3b- and LGM-lake-highstands we reconstructed can tentatively be related to them. Fish remains were basically found throughout the WPS sediment sections, however, during two sub-sections in high abundance (Robbins et al., 2000). We link the strong increase of fish consumption with an outflowing Palaeolake Tsodilo, creating the Tamacha River. Living fish could have reached the palaeolake only by upstream migration via the Tamacha River, which interconnected the lake with the Okavango (Fig. 9). The fish fauna of the Okavango River is diverse and abundant and traditionally represents important nutrition (e.g. Merron, 1993; Mosepele et al., 2009). Robbins et al. (2000) mentioned large bivalves, possibly *Mutela*, collected from the WPS sediments. Such unionid bivalves can slowly migrate upstream as adults but fast and more commonly as larval stage attached to fish (e.g. Fryer, 1961; Graf and Cummings, 2006; Ortiz et al., 2020). A detailed study of the WPS shells could show whether the abundances of fish and unionid bivalves correlate. Although fish remains are low in number before and after the "Lower and Upper Fish" deposits, they indicate that people were adapted to fishing. This baseline fish most likely originated from the Ncamasere River which could be reached in a couple of hours when it was flowing from west to east "long ago" (orally passed indigenous knowledge in Robbins et al., 1994). Nowadays, the Ncamasere is

periodically flooded by the Okavango, but only its lower reaches are affected (e.g. Nash et al., 1997).

Campbell et al. (2010) emphasized the "wealth of edible plants" of Tsodilo. Such knowledge, however, is mainly based on oral communication with recent inhabitants but can hardly be related to ancient times (e.g. Robbins et al., 2010). For the period focused in this study (ca. 43–19 ka), only single Mongongo nuts (from the Manketti tree *Schinziophyton rautanenii*) were noted from WPS (Robbins et al., 2010) and Rhino Cave deposits (Robbins et al., 1996). This is in line with observations from other regions where Mongongo nuts were the major vegetable food, e.g. in sub-recent San camps (Yellen, 1998). It thus can only be speculated to which extent ancient humans of the Tsodilos sustained on gathering fruits. We briefly discuss, however, whether the existence of a lake and related hydroclimate favoured gathering or not. Our preliminary results confirm that vegetation in the lake beds is azonal, differing from the typical sandveld vegetation (e.g. Passarge, 1904; Brook, 2010) by higher diversity and density of shrubs and particularly trees (Fig. 4). This is likely due to lower amounts of sand and the carbonatic duricrusts preventing quick seepage of precipitation. It is noteworthy that the arable farming of the Hambukushu, who have settled at Tsodilo since the 19th century (e.g. Giraudo, 2018), has concentrated on the southern lake depression and is perfectly delimited by the MIS 3b and LGM highstands' shorelines (Fig. 7). The chernozem-like soil we excavated in Pit S2-18 further indicates fertility of lake depression land. Given that ancient humans also sustained on gathering fruits, Palaeolake Tsodilo significantly reduced the area where corresponding plants could grow.

5.3. Vector-borne diseases under changing hydrological settings

Impact of climate change on vector-borne tropical diseases (e.g. Thomson et al., 2018; Fouque and Reeder, 2019) has particularly been discussed in respect of malaria (e.g. Peterson, 2009; Tonnang et al., 2010; Endo and Eltahir, 2018; Moukam Kakmeni, 2018) and schistosomiasis (e.g. Yang and Bergquist, 2018; Adekiya et al., 2020) but also regarding less deadly or less common maladies such as fascioliasis (caused by liver flukes; e.g. Lu et al., 2018; Mahulu et al., 2019) and trypanosomosis (sleeping sickness; Sharma et al., 2001). The vectors of malaria and trypanosomosis are *Anopheles* mosquitos and *Glossina* (Tsetse) flies, respectively (e.g. Bogitsh et al., 2012). While trypanosomosis has been endemic until the 1980s along the Okavango and particularly in its delta (e.g. Sharma et al., 2001), malaria still prevails in northern Botswana (e.g. Sinka et al., 2010). Malaria probably evolved in Africa (e.g. Rich et al., 1998) and possibly reached Eurasia during the out-of-Africa expansions as early as 60,000 years ago (e.g. Gelabert et al., 2017) and later eventually contributed to the fall of the Roman Empire (e.g. Soren, 2003; Sallares et al., 2004), under a climate (e.g. McCormick et al., 2012) favouring *Anopheles* habitats. Tishkoff et al. (2001) concluded that "malaria has had a major impact on humans" only since the Early Holocene, under a warmer and more humid climate. Generally, malaria incidence is correlated with rainfall and temperature (e.g. Mabaso et al., 2006; Jones et al., 2007), which define the geographic extent of *Anopheles* (e.g. Sinka et al., 2010; Gething et al., 2014). An inter-annual study in semi-arid Niger showed that a 16% increase in rainfall led to a 132% increase in mosquito abundance (Bomblies et al., 2008). Warm sunlit lakes and ponds provide optimal breeding habitats for *Anopheles* (e.g. Sinka et al., 2010) and Tishkoff et al. (2001) suggested that Late Stone Age settlements at lake shores could have facilitated the spread of malaria. On the other hand, Webb Jr. (2005) considered a much earlier influence of malaria on the peopling of tropical Africa. Considering the Middle to Late Stone Age people of the Tsodilo Hills, we assume that malaria, and trypanosomosis likely too, became more severe during lake periods, which sustained under increased rainfall and higher humidity, while temperature was possibly not lower than today (Wiese et al., 2020). Our hydromorphological models suggest that even during highstands extended areas of Palaeolake Tsodilo were rather shallow, exhibiting wetland character. The water temperature thus paralleled the tropical air temperature, and abundant breeding sites for *Anopheles* were provided.

Shallow vegetated areas of Palaeolake Tsodilo did also represent habitats for pulmonate gastropods such as *Bulinus, Biomphalaria* and *Radix* (Wiese et al., 2020). *Bulinus* and *Biomphalaria* are intermediate hosts of *Schistosoma* while *Radix* is intermediate host of *Fasciola* (Brown, 1994). Schistosomiasis has its origin in Africa and "human capture" (Despres et al., 1992) occurred earlier than Middle Stone Age (e.g. Wright, 1970; Despres et al., 1992). Based on molecular data, Crellen et al. (2018) suggested that adoption of fishing by humans triggered transmission during ca. 150–110 ka ago. Kloos and David (2002) referred to the fossil record of *Bulinus* and *Biomphalaria*, as an indicator for schistosomiasis risk in ancient human populations. Early documented evidence of schistosomiasis in Africans comes e.g. from ancient Egyptian medical papyri (e.g. Kloos and David, 2002; Di Bella et al., 2018). In respect of public health, schistosomiasis is nowadays the most important water-based disease (e.g. Steinmann et al., 2006; Walz et al., 2015). The optimal water temperature for disease transmission ranges from 22 °C to 27 °C (e.g. Kalinda et al., 2017). African-origin *Schistosoma*, recently re-emerged in southern Europe (e.g. Ramalli et al., 2018) demonstrating temperature tolerance, however. Transmission risk is highest under still-water conditions while in flowing water, the larvae, which emerge from the host snail, have lower chances to penetrate human skin (e.g. Secor, 2014 and references therein). A Lake Victoria study exhibited that about 40% of the school-age children were infected (Kabatereine et al., 2011), which is a comparatively low infection rate, though (e.g. Mtethiwa et al., 2015). This might be due to the fact that a huge lake such as Victoria is more exposed to wind than a small lake or pond, and waves and currents and water mixing are generally stronger. On the other hand, rivers also often comprise stagnant water habitats where transmission risk can be similarly high as in lakes or ponds (e.g. Schwartz et al., 2005). Appleton et al. (2008) reported schistosomiasis from the Okavango Delta and Panhandle including habitats where the Tamacha River terminated. Robbins et al. (2000) noted the potential exposure of Tsodilo people to schistosomiasis. Shells of the vector *Bulinus* were extracted from the sediments of Palaeolake Tsodilo abundantly (Wiese et al., 2020; this study) and we assume that people were at high risk to get infected by *Schistosoma*. Transmission risk was highest during periods of smaller lake (pond) sizes and likely lower during lake highstands with active outflow and size-related, higher water turbulences.

It is possible that the majority of ancient Tsodilo people was co-infected by schistosomiasis and malaria (see e.g. Kabatereine et al., 2011) during lake periods while a drier climate with no lake formation reduced the malaria risk significantly and schistosomiasis was even absent.

6. Conclusions

The Tsodilo Hills were possibly initially reached by early modern humans along the Tamacha palaeo-river, which represented the outflow of Palaeolake Tsodilo during its highstands. Three such periods were identified by remote sensing and sedimentological analyses. The highest lake level could not be dated but is tentatively related with a more humid climate in the Kalahari around 100 ka. Radiocarbon dating revealed that two of the highstands occurred during MIS 3b and LGM. A lake with no outflow existed several thousand years before and after the highstands, indicating that extended periods of higher than modern humidity existed. Possibly the periods during which a lake existed were more extended than the periods when the lake beds were dry. This could be part of the explanation why people have occupied the Tsodilo Hills since a hundred thousand years ago or even earlier. On the other hand, permanent water supply and thus game, fish and edible plants were abundant along the Okavango Panhandle and Delta. Why did groups of ancient humans leave that area? Social conflicts between populations could be one reason but we suppose that ancient humans took particular advantage of the Tsodilo Hills as shelter from weather hazards and as a natural fortress, allowing

better protection against predators and elephants. Additionally, the hills provided sheltered springs and could be used as watch towers to spot game. The area was geologically and hydrologically much calmer than the Okavango Graben with its high seismicity and periodically extreme floods. We consider the Palaeolake Tsodilo highstand periods "Garden of Eden" settings with a stable climate and game and fish in abundance. During periods with a smaller or even no lake there was still enough potable water and game, and the risk of infectious diseases even decreased when there was no standing water. The Tsodilo Hills represented a safe haven where social complexity could increase and a long-term social-ecological resilience be built up. Thus, the ancient people from the Tsodilo Hills are certainly worth consideration in the discussion when and where modern human behaviour began.

Data availability statement

The data that supports the findings of this study are available in the supplementary material of this article.

Declaration of competing interest

The authors declare that they have no known competing financial interests or personal relationships that could have appeared to influence the work reported in this paper.

Acknowledgements

Appendix A. Supplementary data

Supplementary data to this article can be found online at https://doi.org/10.1016/j.qsa.2021.100022.

References

Acharya, A., Das, S., Pan, I., Das, S., 2014. Extending the concept of analogue Butterworth filter for fractional order systems. Signal Process. 94, 409–420.

Adekiya, T.A., Aruleba, R.T., Oyinloye, B.E., Okosun, K.O., Kappo, A.P., 2020. The effect of climate change and the snail-schistosome cycle in transmission and bio-control of schistosomiasis in Sub-Saharan Africa. Int. J. Environ. Res. Publ. Health 17, 181.

Aitchison, J., 1982. The statistical analysis of compositional data. J. Roy. Stat. Soc. 44, 139–177.

Aitchison, J., 1986. The statistical analysis of compositional data. Monographs on Statistics and Applied Probability. Chapman and Hall, London, New York.

Appleton, C.C., Ellery, W.N., Byskov, J., Mogkweetsinyana, S.S., 2008. Epidemic transmission of intestinal schistosomiasis in the seasonal part of the Okavango Delta, Botswana. Ann. Trop. Med. Parasitol. 102, 611–623.

Bailly, C., Fortin, J., Adelinet, M., Hamon, Y., 2019. Upscaling of elastic properties in carbonates: A modelling approach based on a multiscale geophysical data set. J. Geophys. Res.: Solid Earth 124, 13021–13038.

Barton, N., 2006. Rock quality, seismic velocity, attenuation and anisotropy. In: Balkema-proceedings and Monographs in Engineering, Water and Earth Sciences. CRC Press, London.

Bekker, R.P., De Wit, P.V., 1991. Vegetation map of the Republic of Botswana. Soil Mapping and Advisory Services Botswana, Gaborone.

Birsoy, R., 2002. Formation of sepiolite-palygorskite and related minerals from solution. Clay Clay Miner. 50, 736–745.

Blome, M.W., Cohen, A.S., Tryon, C.A., Brooks, A.S., Russell, J., 2012. The environmental context for the origins of modern human diversity: a synthesis of regional variability in African climate 150,000-30,000 years ago. J. Hum. Evol. 62, 563–592.

Bogitsh, B., Carter, C., Oeltmann, T., 2012. Human Parasitology, fourth ed. Academic Press, Elsevier.

Brain, C.K., 1981. The Hunters or the Hunted? An Introduction to African Cave Taphonomy. University of Chicago Press, Chicago.

Bomblies, A., Duchemin, J.-B., Eltahir, E.A.B., 2008. Hydrology of malaria: Model development and application to a Sahelian village. Water Resour. Res. 44 (12) https://doi.org/10.1029/2008WR006917.

Breeze, P.S., Drake, N.A., Groucutt, H.S., Parton, A., Jennings, R.P., White, T.S., Clark-Balzan, L., Shipton, C., Scerri, E.M.L., Stimpson, C.M., Crassard, R., Hilbert, Y., Alsharekh, A., Al-Omari, A., Petraglia, M.D., 2015. Remote sensing and GIS techniques for reconstructing Arabian palaeohydrology and identifying archaeological sites. Quat. Int. 382, 98–119.

Brook, G.A., Haberyan, K.A., de Filippis, S., 1992. Evidence of a shallow lake at Tsodilo Hills, Botswana, 17500 to 15000 yr BP: Further confirmation of a widespread Late Pleistocene humid period in the Kalahari Desert. Palaeoecol. Afr. 23, 165–175.

Brook, G.A., 2010. The paleoenvironment of Tsodilo. In: Campbell, A., Robbins, L., Taylor, Michael (Eds.), Tsodilo Hills - Copper Bracelet of the Kalahari, 30-49. Michigan State University Press, East Lansing.

Brook, G.A., Cowart, J.B., Marais, E., 1996. Wet and dry periods in the southern African summer rainfall zone during the last 300 kyr from speleothem, tufa and sand dune age data. Palaeoecol. Afr. 24, 147–158.

Brook, G.A., Scott, L., Railsback, L.B., Goddard, E.A., 2010. A 35 ka pollen and isotope record of environmental change along the southern margin of the Kalahari from a stalagmite and animal dung deposits in Wonderwerk Cave, South Africa. J. Arid Environ. 74, 870–884.

Brown, D., 1994. Freshwater snails of Africa and their Medical Importance. Taylor & Francis Ltd, pp. 132–248.

Burrough, S.L., 2016. Late Quaternary environmental change and human occupation of the southern African interior. In: Jones, S.C., Stewart, B.A. (Eds.), Africa from MIS 6-2: Population Dynamics and Paleoenvironments. Springer, Dordrecht, pp. 161–174.

Burrough, S.L., Thomas, D.S.G., Singarayer, J.S., 2009. Late Quaternary hydrological dynamics in the Middle Kalahari: Forcing and feedbacks. Earth Sci. Rev. 96, 313–326.

Butterworth, S., 1930. On the theory of filter amplifiers. Wireless Eng. 7, 536–541.

Campbell, A., 2010. Visiting Tsodilo: preparing the imagination. In: Campbell, A., Robbins, L., Taylor, M. (Eds.), Tsodilo Hills - Copper Bracelet of the Kalahari, 16-29. Michigan State University Press, East Lansing.

Cassidy, N.J., 2009. Electrical and magnetic properties of rocks, soils and fluids. In: Jol, H.M. (Ed.), Ground Penetrating Radar: Theory and Applications. Elsevier, Amsterdam, pp. 41–72.

Chan, E.K.F., Timmermann, A., Baldi, B.F., Moore, A.E., Lyons, R.J., Lee, S.-S., Kalsbeek, A.M.F., Petersen, D.C., Rautenbach, H., Förtsch, H.E.A., Bornman, M.S.R., Hayes, V.M., 2019. Human origins in a southern African palaeo-wetland and first migrations. Nature 575, 185–189.

Chase, B.M., 2009. Evaluating the use of dune sediments as a proxy for palaeo-aridity: a southern African case study. Earth Sci. Rev. 93, 31–45.

Chase, B.M., Meadows, M.E., 2007. Late Quaternary dynamics of southern Africa's winter rainfall zone. Earth Sci. Rev. 84, 103–138.

Chevalier, M., Chase, B.M., 2016. Determining the drivers of long-term aridity variability: A southern African case study. J. Quat. Sci. 31, 143–151.

Cole, M.M., Brown, R.C., 1976. The Vegetation of the Ghanzi Area of Western Botswana. J. Biogeogr 3 (3), 169. https://doi.org/10.2307/3038009.

Conway, D., van Garderen, E.A., Deryng, D., Dorling, S., Krueger, T., Landman, W., Lankford, B., Lebek, K., Osborn, T., Ringler, C., Thurlow, J., Zhu, T., Dalin, C., 2015. Climate and southern Africa's water-energy-food nexus. Nat. Clim. Change 5, 837–846.

Cooke, H.J., 1980. Landform evolution in the context of climatic change and neo-tectonism in the Middle Kalahari of north-central Botswana. Trans. Inst. Br. Geogr. 5, 80–99.

Copernicus Climate Change Service, 2019. ERA5 Explorer. European Centre for Medium-Range Weather Forecasts (ECMWF).

Coulthard, T.J., Ramirez, J.A., Barton, N., Rogerson, M., Brücher, T., 2013. Were rivers flowing across the Sahara during the last interglacial? Implications for human migration through Africa. PloS One 8, e74834.

Crellen, T., Allan, F., David, S., Durrant, C., Huckvale, T., Holroyd, N., Emery, A.M., Rollinson, D., Aanensen, D.M., Berriman, M., Webster, J.P., Cotton, J.A., 2018. Whole genome resequencing of the human parasite Schistosoma mansoni reveals population history and effects of selection. Sci. Rep. 6, 20954.

Croudace, I.W., Rindby, A., Rothwell, R.G., 2006. ITRAX: description and evaluation of a new multi-function X-ray core scanner. Geol. Soc. Lond. Spec. Publ. 267, 51–63.

Day, M., Edgett, K.S., Stumbaugh, D., 2019. Ancient stratigraphy preserving a wet-to-dry, fluvio-lacustrine to aeolian transition neat Barth Crater, Arabia Terra, Mars. J. Geophys. Res.: Plan 124, 3402–3421.

De Wit, P.V., Bekker, R.P., 1990. Explanatory note on the land systems map of Botswana. Soil Mapping and Advisory Services Botswana, Gaborone.

Despres, L., Imbert-Establet, D., Combes, C., Bonhomme, F., 1992. Molecular evidence linking hominid evolution to recent radiation of schistosomes (Platyhelminthes: Trematoda). Mol. Phylogenet. Evol. 1, 295–304.

Di Bella, S., Riccardi, N., Giacobbe, D.R., Luzzati, R., 2018. History of schistosomiasis (bilharziasis) in humans: from Egyptian medical papyri to molecular biology on mummies. Pathog. Glob. Health 112, 268–273.

DLR, 2009. TerraSAR-X: Das deutsche Radar-Auge im All / The German Radar Eye in Space. DLR, Bonn.

Doglioni, A., Simeone, V., 2014. Geomorphometric analysis based on discrete wavelet transform. Environ. Earth Sci. 71, 3095–3108.

Drake, N.A., El-Hawat, A.S., Turner, P., Armitage, S.J., Salem, M.J., White, K.H., McLaren, S., 2008. Palaeohydrology of the Fazzan Basin and surrounding regions: the last 7 million years. Palaeogeogr. Palaeoclimatol. Palaeoecol. 263, 131–145.

Endo, N., Eltahir, E.A.B., 2018. Environmental determinants of malaria transmission around the Koka Reservoir in Ethiopia. GeoHealth 2, 104–115.

ESRI, 2018. ArcGIS Pro Version 2.2.4. Environmental Systems Research Institute, Redlands, California, United States.

FAO, 2012. *ETo Calculator*. Land and Water Digital Media Series N°36. Rome, Italy. http://www.fao.org/land-water/databases-and-software/eto-calculator/en/.

Feathers, J.K., 1997. Luminescence dating of sediment samples from White Paintings Rockshelter, Botswana. Quat. Sci. Rev. 16, 321–331.

Fouque, F., Reeder, J.C., 2019. Impact of past and on-going changes on climate and weather on vector-borne diseases transmission: a look at the evidence. BMC Infect. Dis. Poverty 8, 51.

Fryer, G., 1961. The developmental history of *Mutela bourguignati* (Ancey) Bourguignat (Mollusca: Bivalvia). Phil. Trans. Roy. Soc. Lond. 244, 259–298.

Galán, E., Pozo, M., 2011. Palygorskite and sepiolite deposits in continental environments. Description, genetic patterns and sedimentary settings. Dev. Clay Sci. 3, 125–173.

Gasse, F., Chalié, F., Vincens, A., Williams, M.A.J., Williamson, D., 2008. Climatic patterns in equatorial and southern Africa from 30,000 to 10,000 years ago reconstructed from terrestrial and near-shore proxy data. Quat. Sci. Rev. 27, 2316–2340.

Gelabert, P., Olalde, I., de-Dios, T., Civit, S., Lalueza-Fox, C., 2017. Malaria was a weak selective force in ancient Europeans. Sci. Rep. 7, 1377.

Gething, P.W., Battle, K.E., Bhatt, S., Smith, D.L., Eisele, T.P., Cibulskis, R.E., Hay, S.I., 2014. Declining malaria in Africa: improving the measurement of progress. Malar. J. 13, 39. https://doi.org/10.1186/1475-2875-13-39.

Gibbons, A., 2019. Experts Question Study Claiming to Pinpoint Birthplace of All Humans. https://doi.org/10.1126/science.aba0155.

Giraudo, R.F., 2018. Heteroglossic heritage and the first-place of the Kalahari. Int. J. Herit. Stud. 24, 128–141.

Goetz, A.F., Vane, G., Solomon, J.E., Rock, B.N., 1985. Imaging spectrometry for Earth remote sensing. Science 228, 1147–1153.

Graf, D.L., Cummings, K.S., 2006. Freshwater mussels (Mollusca: Bivalvia: Unionida) of Angola, with description of a new species, Mutela wistarmorrisi. Proc. Acad. Nat. Sci. Phila. 155, 163–194.

Grove, A.T., 1969. Landforms and climatic change in the Kalahari and Ngamiland. Geogr. J. 135, 191–212.

Harding, A.E., Forrest, M.D., 1989. Analysis of multiple geological datasets from the English Lake District. IEEE Trans. Geosci. Rem. Sens. 27, 732–739.

Hartmann, K., Wünnemann, B., 2009. Hydrological changes and Holocene climate variations in NW China, inferred from lake sediments of Juyanze palaeolake by factor analyses. Quat. Int. 194, 28–44.

Heine, K., 1982. The main stages of the Late Quaternary evolution of the Kalahari region, southern Africa. Palaeoecol. Afr. 15, 53–76.

Heine, K., 2019. Das Quartär in den Tropen - Eine Rekonstruktion des Paläoklimas. Springer, Berlin.

Heiri, O., Lotter, A.F., Lemcke, G., 2001. Loss on ignition as a method for estimating organic and carbonate content in sediments: reproducibility and comparability of results. J. Paleolimnol. 25, 101–110.

Henn, B.M., Gignoux, C.R., Jobin, M., Granka, J.M., Macpherson, J.M., Kidd, J.M., Rodríguez-Botigué, L., Ramachandran, S., Hon, L., Brisbin, A., Lin, A.A., Underhill, P.A., Comas, D., Kidd, K.K., Norman, P.J., Parham, P., Bustamante, C.D., Mountain, J.L., Feldman, M.W., 2011. Hunter-gatherer genomic diversity suggests a southern African origin for modern humans. Proc. Natl. Acad. Sci. U.S.A. 108, 5154–5162.

Henshilwood, C.S., d'Errico, F., van Niekerk, K.L., Coquinot, Y., Jacobs, Z., Lauritzen, S.-E., Menu, M., García-Moreno, R., 2011. A 100,000-year-old ochre-processing workshop at Blombos Cave, South Africa. Science 334, 219.

Hogg, A.G., Heaton, T.J., Hua, Q., Palmer, J.G., Turney, C.S.M., Southon, J., Bayliss, A., Blackwell, P.G., Boswijk, G., Bronk Ramsey, C., Pearson, C., Petchey, F., Reimer, P., Reimer, R., Wacker, L., 2020. SHCal20 Southern Hemisphere calibration, 0–55,000 years cal BP. Radiocarbon 1–20.

Hollister, J.W., 2018. *Lakemorpho: Lake Morphometry Metrics*. R Package Version 1.1.1. URL: https://CRAN.R-project.org/package=lakemorpho.

Hollister, J.W., Stachelek, J., 2017. lakemorpho: calculating lake morphometry metrics in R. F1000Research 6, 1718.

Hunt, G.R., 1980. Electromagnetic radiation: the communication link in remote sensing. In: Siegal, B.S., Gillespie, A.R. (Eds.), Remote Sensing in Geology. Wiley, New York, pp. 5–45.

Hutchins, D.G., Hutton, L.G., Hutton, S.M., Jones, C.R., Loenhert, E.P., 1976. A summary of the geology, seismicity, geomorphology and hydrogeology of the Okavango Delta. Bulletin 7 Geological Survey, Lobatse, Botswana.

Imbroane, M.A., Melenti, C., Gorgan, D., 2007. Mineral explorations by Landsat image ratios. In: IEEE Computer Society (Ed.), Proceedings of the 9th International Symposium on Symbolic and Numeric Algorithms for Scientific Computing, SYNASC 2007. IEEE, Piscataway, NJ, pp. 335–340.

Ivester, A.H., Brook, G.A., Robbins, L.H., Campbell, A.C., Murphy, M.L., Marais, E., 2010. A sedimentary record of environmental change at Tsodilo Hills White Paintings Rock Shelter, Northwest Kalahari Desert, Botswana. Palaeoecol. Afr. 30, 53–78.

Izzawati, Wallington, E.D., Woodhouse, I.H., 2006. Forest height retrieval from commercial X-band SAR products. IEEE Trans. Geosci. Rem. Sens. 44, 863–870.

Jahn, B., Donner, B., Müller, P.J., Röhl, U., Schneider, R.R., Wefer, G., 2003. Pleistocene variations in dust input and marine productivity in the northern Benguela Current: Evidence of evolution of global glacial-interglacial cycles. Palaeogeogr. Palaeoclimatol. Palaeoecol. 193, 515–533.

Jones, A.E., Uddenfeldt Wort, U., Morse, A.P., Hastings, I.M., Gagnon, A.S., 2007. Climate prediction of El Nino malaria epidemics in north-west Tanzania. Malar. J. 6, 162.

Kabatereine, N.B., Standley, C.J., Sousa-Figueiredo, J.C., Fleming, F.M., Stothard, J.R., Talisuna, A., Fenwick, A., 2011. Integrated prevalence mapping of schistosomiasis, soil-transmitted helminthiasis and malaria in lakeside and island communities in Lake Victoria, Uganda. BMC Parasites Vectors 4, 232.

Kalbermatten, M., van de Ville, D., Turberg, P., Tuia, D., Joost, S., 2012. Multiscale analysis of geomorphological and geological features in high resolution digital elevation models using the wavelet transform. Geomorphology 138, 352–363.

Kalinda, C., Chimbari, M.J., Mukaratirwa, S., 2017. Effect of temperature on the *Bulinus globosus* — *Schistosoma haematobium* system. BMC Infect. Dis. Poverty 6, 57.

Karaman, S., Yeken, T., 2008. Determination of physical properties of carbonate rocks from P-wave velocity. Bull. Eng. Geol. Environ. 67, 277–281.

Kearey, P., Brooks, M., Hill, I., 2002. An Introduction to Geophysical Exploration. Blackwell Science, Oxford.

Key, R.M., Ayres, N., 2000. The 1998 edition of the national geological map of Botswana. J. Afr. Earth Sci. 30, 427–451.

Kinabo, B.D., Atekwana, E.A., Hogan, J.P., Modisi, M.P., Wheaton, D.D., Kampunzu, A.B., 2007. Early structural development of the Okavango rift zone, NW Botswana. J. Afr. Earth Sci. 48, 125–136.

Kloos, H., David, R., 2002. The paleoepidemiology of schistosomiasis in ancient Egypt. Hum. Ecol. Rev. 9, 14–25.

Lancaster, N., 1981. Paleoenvironmental implications of fixed dune systems in Southern Africa. Palaeogeogr. Palaeoclimatol. Palaeoecol. 33, 327–346.

Linol, B., Wit, M. J. de, Guillocheau, F., Wit, M. C. J. de, Anka, Z., Colin, J.-P., 2015. Formation and collapse of the Kalahari duricrust ['African Surface'] across the Congo Basin, with implications for changes in rates of Cenozoic off-shore sedimentation. In: De Wit, M.J., Guillocheau, F., De Wit, M.C.J. (Eds.), Geology and Resource Potential of the Congo Basin, 193-210. Springer, Berlin.

Loelkes Jr., G.L., Howard Jr., G.E., Schwertz Jr., E.L., Lampert, P.D., Miller, S.W., 1983. Land use/land cover and environmental photointerpretation keys. US Geol. Surv. Bull. 1600.

Lu, X.T., Gu, Q.Y., Limpanont, Y., Song, L.G., Wu, Z.D., Okanurak, K., Lv, Z.Y., 2018. Snail-borne parasitic diseases: an update on global epidemiological distribution, transmission interruption and control methods. BMC Infect. Dis. Poverty 7, 28.

Mabaso, M.L.H., Vounatsou, P., Midzi, S., Da Silva, J., Smith, T., 2006. Spatio-temporal analysis of the role of climate in inter-annual variation of malaria incidence in Zimbabwe. BMC Int. J. Health Geogr. 5, 20.

Mahulu, A., Clewing, C., Stelbrink, B., Chibwana, F.D., Tumwebaze, I., Stothard, J.R., Albrecht, C., 2019. Cryptic intermediate snail host of the liver fluke Fasciola hepatica in Africa. BMC Parasites Vectors 12, 573.

Martín-Fernandez, J.A., Barcelo-Vidal, C., Pawlowsky-Glahn, V., 2000. Zero replacement in compositional data sets. In: Kiers, H.A.L., Rasson, J., Groenen, P.J.F., Schader, M. (Eds.), Data Analysis, Classification, and Related Methods. Studies in Classification, Data Analysis, and Knowledge Organization. Springer, Berlin, pp. 155–160.

McCall, G.S., Thomas, J.T., 2009. Re-examining the South African middle-to-later stone age transition: Multivariate analysis of the Umhlatuzana and rose cottage cave stone tool assemblages. Azania 44, 311–330.

McCormick, M., Büntgen, U., Cane, M.A., Cook, E.R., Harper, K., Huybers, P., Litt, T., Manning, S.W., Mayewski, P.A., More, A.F.M., Nicolussi, K., Tegel, W., 2012. Climate change during and after the Roman Empire: Reconstructing the past from scientific and historical evidence. J. Interdiscipl. Hist. 43, 169–220.

McFarlane, M.J., Eckardt, F.D., 2007. Palaeodune morphology associated with the Gumare fault of the Okavango graben in the Botswana/Namibia borderland: a new model of tectonic influence. S. Afr. J. Geol. 110, 535–542.

McGee, D., Donohoe, A., Marshall, J., Ferreira, D., 2014. Changes in ITCZ location and cross-equatorial heat transport at the last glacial maximum, Heinrich Stadial 1, and the mid-Holocene. Earth Planet Sci. Lett. 390, 69–79.

Mentzer, S.M., 2017. Rockshelter setting. In: Gilbert, A.S. (Ed.), Encyclopedia of Geoarchaeology, 725-743. Encyclopedia of Earth Sciences Series. Springer, Dordrecht.

Merron, G.S., 1993. A synopsis of presentations and discussions on the fish and fishery in the Okavango Delta, Botswana. Botsw. Notes Rec. 25, 133–140.

Michczyński, A., 2007. Is it possible to find a good point estimate of a calibrated radiocarbon date? Radiocarbon 49, 393–401.

Mmualefe, L.C., Torto, N., 2011. Water quality in the Okavango Delta. Water SA 37, 411–418.

Modisi, M.P., Atekwana, E.A., Kampunzu, A.B., Ngwisanyi, T.H., 2000. Rift kinematics during the incipient stages of continental extension: Evidence from nascent Okavango rift basin, northwest Botswana. Geology 28 (10), 939–942.

Mosepele, K., Moyle, P.B., Merron, G.S., Purkey, D.R., Mosepele, B., 2009. Fish, floods, and ecosystem engineers: Aquatic conservation in the Okavango Delta, Botswana. Bioscience 59, 53–64.

Moukam Kakmeni, F.M., Guimapi, R.Y.A., Ndjomatchoua, F.T., Pedro, S.A., Mutunga, J., Tonnang, H.E.Z., 2018. Spatial panorama of malaria prevalence in Africa under climate change and interventions scenarios. BMC Int. J. Health Geogr. 17, 2.

Mtethiwa, A.H.N., Nkwengulila, G., Bakuza, J., Sikawa, D., Kazembe, A., 2015. Extent of morbidity associated with schistosomiasis infection in Malawi: a review paper. BMC Infect. Dis. Poverty 4, 25.

Nash, D.J., Meadows, M.E., Shaw, P.A., Baxter, A.J., Gieske, A., 1997. Late Holocene sedimentation rates and geomorphological significance of the Ncamasere Valley, Okavango Delta, Botswana. S. Afr. Geogr. J. 93–100.

Nash, D.J., Meadows, M.E., Gulliver, V.L., 2006. Holocene environmental change in the Okavango Panhandle, northwest Botswana. Quat. Sci. Rev. 25, 1302–1322.

Nthaba, B., Simon, R.E., Ogubazghi, G.M., 2018. Seismicity study of Botswana from 1966 to 2012. Int. J. Geosci. 9, 707–718.

Ntibinyane, O., Kwadiba, M.T., Maritinkole, J., Kelepile, P., 2019. Seismicity of the Okavango Delta Region: Contribution of IMS and Local Stations. Poster CTBT Science and Technology Conference, Vienna, Austria.

Okada, K., Segawa, K., Hayashi, I., 1993. Removal of the vegetation effect from LANDSAT TM and GER imaging spectroradiometer data. ISPRS J. Photogrammetry Remote Sens. 48, 16–27.

Oleś, A., Pau, G., Smith, M., Sklyar, O., Huber, Barry, J., Marais, P.A., 2018. *EBImage: Image Processing and Analysis Toolbox for R*. R Package version 4.22.1. URL: htt ps://github.com/aoles/EBImage.

Ortiz-Sepulveda, C.M., Stelbrink, B., Vekemans, X., Albrecht, C., Riedel, F., Todd, J.A., Van Bocxlaer, B., 2020. Diversification dynamics of freshwater bivalves (Unionidae: Parreysiinae: Coelaturini) indicate historic hydrographic connections throughout the East African Rift System. Mol. Phylogenet. Evol. 148, 106816.

Passarge, S., 1904. Die Kalahari. Dietrich Reimer, Berlin.

Pau, G., Fuchs, F., Sklyar, O., Boutros, M., Huber, W., 2010. EBImage - an R package for image processing with applications to cellular phenotypes. Bioinformatics 26, 979–981.

Peel, M.C., Finlayson, B.L., McMahon, T.A., 2007. Updated world map of the Köppen-Geiger climate classification. Hydrol. Earth Syst. Sci. 11, 1633–1644.

Percival, J.B., White, H.P., Goodwin, T.A., Parsons, M.B., Smith, P.K., 2014. Mineralogy and spectral reflectance of soils and tailings from historical gold mines, Nova Scotia. Geochem. Explor. Environ. Anal. 14, 3–16.

Perko, R., Raggam, H., Deutscher, J., Gutjahr, K., Schardt, M., 2011. Forest assessment using high resolution SAR data in X-band. Rem. Sens. 3, 792–815.

Peterson, A.T., 2009. Shifting suitability for malaria vectors across Africa with warming climates. BMC Infect. Dis. 9, 59.

Pipaud, I., Loibl, D., Lehmkuhl, F., 2015. Evaluation of TanDEM-X elevation data for geomorphological mapping and interpretation in high mountain environments - A case study from SE Tibet, China. Geomorphology 246, 232–254.

Pozo, M., Calvo, J.P., 2018. An overview of authigenic magnesian clays. Minerals 8, 520.

Ramalli, L., Noël, H., Chiappini, J.D., Vincent, J., Barré-Cardi, H., Malfait, P., Normand, G., Busato, F., Gendrin, V., Mulero, S., Allienne, J.F., Fillaux, J., Boissier, J., Berry, A., 2018. A persistent risk of urogenital schistosomiasis transmission linked to the Cavu River in Southern Corsica since 2013. Revue d'Épidémiologie et de Santé Publique 66, S258–S259.

R Core Team, 2019. R: A Language and Environment for Statistical Computing. R Foundation for Statistical Computing, Vienna, Austria. URL: https://www.R-project.o rg/.

Rich, S.M., Licht, M.C., Hudson, R.R., Ayala, F.J., 1998. Malaria's Eve: Evidence of a recent population bottleneck throughout the world populations of *Plasmodium falciparum*. Proc. Natl. Acad. Sci. Unit. States Am. 95, 4425–4430.

Richter, T.O., van der Gaast, S., Koster, B., Vaars, A., Gieles, R., Stigter, H. C. de, Haas, H. de, van Weering, T.C.E., 2006. The Avaatech XRF Core Scanner: technical description and applications to NE Atlantic sediments. Geol. Soc. Lond. Spec. Publ. 267, 39–50.

Riedel, F., Henderson, A.C.G., Heußner, K.-U., Kaufmann, G., Kossler, A., Leipe, C., Shemang, E., Taft, L., 2014. Dynamics of a Kalahari terminal mega-lake system: hydromorphological and limnological changes in the Makgadikgadi Basin (Botswana) during the terminal 50 ka. Hydrobiologia 739, 25–53.

Ringrose, S., Huntsman-Mapila, P., Downey, W., Coetzee, S., Fey, M., Vanderpost, C., Vink, B., Kemosidile, T., Kolokose, D., 2008. Diagenesis in Okavango fan and adjacent dune deposits with implications for the record of palaeo-environmental change in Makgadikgadi–Okavango–Zambezi basin, northern Botswana. Geomorphology 101, 544–557.

Rito, T., Vieira, D., Silva, M., Conde-Sousa, E., Pereira, L., Mellars, P., Richards, M.B., Soares, P., 2019. A dispersal of *Homo sapiens* from southern to eastern Africa immediately preceded the out-of-Africa migration. Sci. Rep. 9, 4728.

Rizzoli, P., Martone, M., Gonzalez, C., Wecklich, C., Borla Tridon, D., Bräutigam, B., Bachmann, M., Schulze, D., Fritz, T., Huber, M., Wessel, B., Krieger, G., Zink, M., Moreira, A., 2017. Generation and performance assessment of the global TanDEM-X digital elevation model. ISPRS J. Photogrammetry Remote Sens. 132, 119–139.

Robbins, L.H., Murphy, M.L., 2011. An overview of the Later and Middle Stone Age at Tsodilo Hills. Botsw. Notes Rec. 43, 130–139.

Robbins, L.H., Brook, G.A., Murphy, M.L., Ivester, A.H., Campbell, A.C., 2016. The Kalahari during MIS 6-2 (190–12 ka): archaeology, paleoenvironment, and population dynamics. In: Jones, S.C., Stewart, B.A. (Eds.), Africa from MIS 6-2: Population Dynamics and Paleoenvironments. Springer, Dordrecht, pp. 175–193.

Robbins, L.H., Murphy, M.L., Brook, G.A., Ivester, A.H., Campbell, A.C., Klein, R.G., Milo, R.G., Stewart, K.M., Downey, W.S., Stevens, N.J., 2000. Archaeology, palaeoenvironment, and chronology of the Tsodilo Hills White Paintings Rock Shelter, northwest Kalahari Desert, Botswana. J. Archaeol. Sci. 27, 1085–1113.

Robbins, L.H., Murphy, M., Campbell, A., 2010. Windows into the past: excavating Stone Age shelters. In: Campbell, A., Robbins, L., Taylor, M. (Eds.), *Tsodilo Hills - Copper Bracelet of the Kalahari, 50–63*. Michigan State University Press, East Lansing.

Robbins, L.H., Murphy, M.L., Campbell, A.C., Brook, G.A., 1996. Excavations at the Tsodilo Hills Rhino Cave. Botsw. Notes Rec. 28, 23–45.

Robbins, L.H., Murphy, M.L., Stewart, K.M., Campbell, A.C., Brook, G.A., 1994. Barbed bone points, paleoenvironment, and the antiquity of fish exploitation in the Kalahari Desert, Botswana. J. Field Archaeol. 21, 257–264.

Rodriguez, F., Maire, E., Courjault-Radé, P., Darrozes, J., 2002. The Black Top Hat function applied to a DEM: A tool to estimate recent incision in a mountainous watershed (Estibère Watershed, Central Pyrenees). Geophys. Res. Lett. 29, 9-1–9-4.

Sabins, F.F., 1999. Remote sensing for mineral exploration. Ore Geol. Rev. 14, 157–183.

Sallares, R., Bouwman, A., Anderung, C., 2004. The spread of malaria to southern Europe in antiquity: new approaches to old problems. Med. Hist. 48, 311–328.

Salzburger, W., Meyer, A., 2004. The species flocks of East African cichlid fishes: recent advances in molecular phylogenetics and population genetics. Naturwissenschaften 91, 277–290.

Sandmeier, K.J., 2017. REFLEXW, Version 8.5. Windows™ XP/7/8/10-program for the processing of seismic, acoustic or electromagnetic reflection, refraction and transmission data. Sandmeier Geophys. Res.

Scerri, E.M.L., Thomas, M.G., Manica, A., Gunz, P., Stock, J.T., Stringer, C., Grove, M., Groucutt, H.S., Timmermann, A., Rightmire, G.P., d'Errico, F., Tryon, C.A., Drake, N.A., Brooks, A.S., Dennell, R.W., Durbin, R., Henn, B.M., Lee-Thorp, J., deMenocal, P., Petraglia, M.D., Thompson, J.C., Scally, A., Chikhi, L., 2018. Did our species evolve in subdivided populations across Africa, and why does it matter? Trends Ecol. Evol. 33, 582–594.

Schmidt, M., Fuchs, M., Henderson, A.C.G., Kossler, A., Leng, M.J., Mackay, A.W., Shemang, E., Riedel, F., 2017. Paleolimnological features of a mega-lake phase in the Makgadikgadi Basin (Kalahari, Botswana) during marine isotope stage 5 inferred from diatoms. J. Paleolimnol. 58, 373–390.

Schneider, W.A., 1978. Integral formulation for migration in 2 and 3 dimensions. Geophysics 43, 49–76.

Schneider, T., Bischoff, T., Haug, G.H., 2014. Migrations and dynamics of the intertropical convergence zone. Nature 513, 45–53.

Schulze, D., Zink, M., Krieger, G., Fiedler, H., Böer, J., Moreira, A., 2008. TanDEM-X: TerraSAR-X Add-On for Digital Elevation Measurements. Jahreskongress Nutzung des Weltraums, Berlin, Germany.

Schumann, G.J.-P., Moller, D.K., 2015. Microwave remote sensing of flood inundation. Phys. Chem. Earth, Parts A/B/C 83–84, 84–95.

Schuster, M., Roquin, C., Duringer, P., Brunet, M., Caugy, M., Fontugne, M., Taïsso Mackaye, H., Vignaud, P., Ghienne, J.-F., 2005. Holocene Lake Mega-Chad palaeoshorelines from space. Quat. Sci. Rev. 24, 1821–1827.

Schuster, S.C., Miller, W., Ratan, A., Tomsho, L.P., Giardine, B., Kasson, L.R., Harris, R.S., Petersen, D.C., Zhao, F., Qi, J., Alkan, C., Kidd, J.M., Sun, Y., Drautz, D.I., Bouffard, P., Muzny, D.M., Reid, J.G., Nazareth, L.V., Wang, Q., Burhans, R., Riemer, C., Wittekindt, N.E., Moorjani, P., Tindall, E.A., Danko, C.G., Teo, W.S., Buboltz, A.M., Zhang, Z., Ma, Q., Oosthuysen, A., Steenkamp, A.W., Oostuisen, H., Venter, P., Gajewski, J., Zhang, Y., Pugh, B.F., Makova, K.D., Nekrutenko, A., Mardis, E.R., Patterson, N., Pringle, T.H., Chiaromonte, F., Mullikin, J.C., Eichler, E.E., Hardison, R.C., Gibbs, R.A., Harkins, T.T., Hayes, V.M., 2010. Complete Khoisan and Bantu genomes from southern Africa. Nature 463, 943–947.

Schwartz, E., Kozarsky, P., Wilson, M., Cetron, M., 2005. Schistosome infection among river rafters on Omo River, Ethiopia. J. Trav. Med. 12, 3–8.

Secor, W.E., 2014. Water-based interventions for schistosomiasis control. Pathog. Glob. Health 108, 246–254.

Segadika, P., 2006. Managing intangible heritage at Tsodilo. Mus. Int. 58, 31–40.

Sharma, S.P., Losho, T.C., Malau, M., Mangate, K.G., Linchwe, K.B., Amanfu, W., Motsu, T.K., 2001. The resurgence of trypanosomosis in Botswana. J. S. Afr. Vet. Assoc. 72, 232–234.

Shemang, E.M., Molwalefhe, L.N., 2011. Geomorphic landforms and tectonism along the eastern margin of the Okavango Rift Zone, north-western Botswana as deduced from geophysical data in the area. In: Sharkov, E.V. (Ed.), New Frontiers in Tectonic Research: General Problems, Sedimentary Basins and Island Arcs. InTech, Rijeka, Croatia.

Sianga, K., Fynn, R., 2017. The vegetation and wildlife habitats of the Savuti-Mababe-Linyanti ecosystem, northern Botswana. Koedoe 59, a1406.

Singer, A., 1979. Palygorskite in sediments: detrital, diagenetic or neoformed – a critical review. Geol. Rundsch. 68, 996–1008.

Singletary, S.J., Hanson, R.E., Martin, M.W., Crowley, J.L., Bowring, S.A., Key, R.M., Ramokate, L.V., Direng, B.B., Krol, M.A., 2003. Geochronology of basement rocks in the Kalahari Desert, Botswana, and implications for regional Proterozoic tectonics. Precambrian Res. 121, 47–71.

Sinka, M.E., Bangs, M.J., Manguin, S., Coetzee, M., Mbogo, C.M., Hemingway, J., Patil, A.P., Temperley, W.H., Gething, P.W., Kabaria, C.W., Okara, R.M., Van Boeckel, T., Godfray, H.C.J., Harbach, R.E., Hay, S.I., 2010. The dominant *Anopheles* vectors of human malaria in Africa, Europe and the Middle East: occurrence data, distribution maps and bionomic précis. BMC Parasites Vectors 3, 117.

Soren, D., 2003. Can archaeologists excavate evidence of malaria? World Archaeol. 35, 193–209.

Sparks, J., Smith, W., 2005. Freshwater fishes, dispersal ability, and nonevidence: "Gondwana Life Rafts" to the rescue. Syst. Biol. 54, 158–165.

Spinage, C.A., 2012. African Ecology: Benchmarks and Historical Perspectives. Springer, Berlin.

Staurset, S., Coulson, S., 2014. Sub-surface movement of stone artefacts at White Paintings Shelter, Tsodilo Hills, Botswana: implications for the Middle Stone Age chronology of central southern Africa. J. Hum. Evol. 75, 153–165.

Steinmann, P., Keiser, J., Bos, R., Tanner, M., Utzinger, J., 2006. Schistosomiasis and water resources development: systematic review, meta-analysis, and estimates of people at risk. Lancet Infect. Dis. 6, 411–425.

Stringer, C., Galway-Witham, J., 2017. Palaeoanthropology: on the origin of our species. Nature 546, 212–214.

Stuiver, M., Reimer, P.J., 1993. Extended ^{14}C data base and revised CALIB 3.0 ^{14}C age calibration program. Radiocarbon 35, 215–230.

Stuiver, M., Reimer, P.J., 2020. CALIB: Radiocarbon Calibration Program Version Rev 8.1.0.

Tanase, M.A., Ismail, I., Lowell, K., Karyanto, O., Santoro, M., 2015. Detecting and quantifying forest change: the potential of existing C- and X-band radar datasets. PloS One 10, e0131079.

The MathWorks, Inc, 2015a. MATLAB Version R2015a—8.4.0.197613. Natick, Massachusetts, United States.

The MathWorks, Inc, 2015b. Wavelet Toolbox Version 4.14.1. Natick, Massachusetts, United States.

Thomas, D.S.G., Brook, G.A., Shaw, P.A., Bateman, M.D., Haberyan, K.A., Appleton, C., Nash, D.J., McLaren, S., Davies, F., 2003. Late Pleistocene wetting and drying in the NW Kalahari: an integrated study from the Tsodilo Hills, Botswana. Quat. Int. 104, 53–67.

Thomas, D.S.G., Burrough, S.L., 2016. Luminescence-based dune chronologies in southern Africa: analysis and interpretation of dune database records across the subcontinent. Quat. Int. 410, 30–45.

Thomson, M.C., Munoz, Á.G., Cousin, R., Shumake-Guillemot, J., 2018. Climate drivers of vector-borne diseases in Africa and their relevance to control programmes. BMC Infect. Dis. Poverty 7, 81.

Timmermann, A., Friedrich, T., 2016. Late Pleistocene climate drivers of early human migration. Nature 538, 92–95.

Tishkoff, S.A., Reed, F.A., Friedlaender, F.R., Ehret, C., Ranciaro, A., Froment, A., Hirbo, J.B., Awomoyi, A.A., Bodo, J.-M., Doumbo, O., Ibrahim, M., Juma, A.T., Kotze, M.J., Lema, G., Moore, J.H., Mortensen, H., Nyambo, T.B., Omar, S.A., Powell, K., Pretorius, G.S., Smith, M.W., Thera, M.A., Wambebe, C., Weber, J.L., Williams, S.M., 2009. The genetic structure and history of Africans and African Americans. Science 324, 1035–1044.

Tishkoff, S.A., Varkonyi, R., Cahinhinan, N., Abbes, S., Argyropoulos, G., Destro-Bisol, G., Drousiotou, A., Dangerfield, B., Lefranc, G., Loiselet, J., Piro, A., Stoneking, M., Tgarelli, A.Q., Tagarelli, G., Touma, E.H., Williams, S.M., Clark, A.G., 2001. Haplotype diversity and linkage disequilibrium at Human *G6PD*: recent origin of alleles that confer malaria resistance. Science 293, 455–462.

Tonnang, H.E.Z., Kangalawe, R.Y.M., Yanda, P.Z., 2010. Predicting and mapping malaria under climate change scenarios: the potential redistribution of malaria vectors in Africa. Malar. J. 9, 111.

van den Boogaart, K. Gerald, Tolosana-Delgado, R., Bren, M., 2020. Compositions: Compositional Data Analysis. R Package Version 1.40-5. URL: https://CRAN.R-proj ect.org/package=compositions

van Wyk, B., van Wyk, P., 1997. Field Guide to Trees of Southern Africa. Struik Publishers, Cape Town.

Villa, P., Soriano, S., Tsanova, T., Degano, I., Higham, T.F.G., d'Errico, F., Backwell, L., Lucejko, J.J., Colombini, M.P., Beaumont, P.B., 2012. Border cave and the beginning of the later stone age in South Africa. Proc. Natl. Acad. Sci. U.S.A. 109, 13208–13213.

Vlag, P.A., Kruiver, P.P., Dekkers, M.J., 2004. Evaluating climate change by multivariate statistical techniques on magnetic and chemical properties of marine sediments (Azores region). Palaeogeogr. Palaeoclimatol. Palaeoecol. 212, 23–44.

Walz, I., Wegmann, M., Dech, S., Raso, G., Utzinger, J., 2015. Risk profiling of schistosomiasis using remote sensing: approaches, challenges and outlook. BMC Parasites Vectors 8, 163.

Weaver, T.D., 2012. Did a discrete event 200,000-100,000 years ago produce modern humans? J. Hum. Evol. 63, 121–126.

Webb Jr., J.L.A., 2005. Malaria and the peopling of early tropical Africa. J. World Hist. 16, 269–291.

Weltje, G.J., Tjallingii, R., 2008. Calibration of XRF core scanners for quantitative geochemical logging of sediment cores: theory and application. Earth Planet Sci. Lett. 274, 423–438.

Wendorff, M., 2005. Outline of lithostratigraphy, sedimentation and tectonics of the Tsodilo Hills group, a neoproterozoic-lower palaeozoic siliciclastic succession in NW Botswana. Ann. Soc. Geol. Pol. 75, 17–25.

Wessel, B., Huber, M., Wohlfart, C., Marschalk, U., Kosmann, D., Roth, A., 2018. Accuracy assessment of the global TanDEM-X digital elevation model with GPS data. ISPRS J. Photogrammetry Remote Sens. 139, 171–182.

Weydahl, D.J., Sagstuen, J., Dick, Ø.B., Rønning, H., 2007. SRTM DEM accuracy assessment over vegetated areas in Norway. Int. J. Rem. Sens. 28, 3513–3527.

Wiese, R., Hartmann, K., Gummersbach, V.S., Shemang, E., Struck, U., Riedel, F., 2020. Lake highstands in the northern Kalahari, Botswana, during MIS 3b and LGM. Quat. Int. 558, 10–18 (in press).

Wright, C.A., 1970. The ecology of African schistosomiasis." Symposia of the Society for the Study of Human Biology, Vol. 9. Human ecology in the tropics. Oxford, England. Pergamon Press.

Wünnemann, B., Demske, D., Tarasov, P., Kotlia, B.S., Reinhardt, C., Bloemendal, J., Diekmann, B., Hartmann, K., Krois, J., Riedel, F., 2010. Hydrological evolution during the last 15 kyr in the Tso Kar lake basin (Ladakh, India), derived from geomorphological, sedimentological and palynological records. Quat. Sci. Rev. 29, 1138–1155.

Yang, G.J., Bergquist, R., 2018. Potential impact of climate change on schistosomiasis: a global assessment attempt. Trop. Med. Infect. Dis. 3, 117.

Yazdi, M., Taheri, M., Navi, P., Sadati, N., 2013. Landsat ETM+ imaging for mineral potential mapping: application to Avaj area, Qazvin, Iran. Int. J. Rem. Sens. 34, 5778–5795.

Yellen, J.E., 1998. Settlement patterns of the !Kung: an archaeological perspective. In: Lee, R.B., DeVore, I. (Eds.), Kalahari Hunter-Gatherers. Studies of the !Kung San and Their Neighbors. Harvard University Press, London, pp. 47–72.